

# **Metabolic Patterns of Corticobasal Syndrome: Differentiating Underlying Pathology Using [<sup>18</sup>F]FDG-PET**

A dissertation submitted to The University of Manchester for the degree of MSc  
Neuroimaging for Clinical and Cognitive Neuroscience in the Faculty of Biology,  
Medicine and Health.

**2025**

**11475102**

**School of Health Sciences**

## Contents

Abbreviations .....	4
List of Figures .....	6
List of Tables .....	7
Abstract .....	8
Declaration .....	9
Intellectual Property Statement .....	10
Acknowledgements .....	11
1. Literature Review .....	12
1.1 Principles of Cerebral Glucose Metabolism in FDG-PET .....	12
1.1.1 Glucose transport and utilisation .....	12
1.1.2 [ <sup>18</sup> F]FDG uptake and PET quantification .....	13
1.1.3 FDG-PET limitations and image analysis approaches .....	13
1.2 CBS and underlying pathologies .....	16
1.2.1 Clinical Heterogeneity and Diagnostic Challenges .....	16
1.2.2 Neuropathology of CBD and AD .....	20
1.2.3 Neuroimaging signatures of CBS pathologies .....	21
1.3 Aims and hypotheses .....	24
2. Methods .....	25
2.1 Participants .....	25
2.2 Clinical and Neuropsychological Assessments .....	25
2.3 Imaging Acquisition .....	26
2.3.1 FDG-PET .....	26
2.3.2 Structural MRI .....	27
2.4 Image Analysis .....	27
2.4.1 Pre-processing .....	29
2.4.2 Compartmental Modelling .....	30
2.4.3 Spectral Analysis .....	32
2.4.4 Quantification of Cerebral Glucose Metabolism .....	32
2.5 Statistical analysis .....	33
2.5.1 VOI Analysis .....	33
2.5.2 Voxel-wise Analysis .....	35

3. Results.....	37
3.1 VOI Analysis.....	38
3.2 Voxel-wise Analysis .....	42
4. Discussion .....	44
4.1 Patients versus Controls .....	44
4.2 CBS-AD versus CBS-CBD .....	46
4.3 VOI and Voxel-Wise Analysis .....	47
4.4 Strengths and limitations .....	48
4.5 Future Directions .....	50
4.6 Clinical and Theoretical Implications .....	52
4.7 Conclusion .....	54
5. References .....	55

**Word Count: 9974**

## Abbreviations

[ <sup>18</sup> F]FDG-PET	Fluorine-18 Fluorodeoxyglucose Positron Emission Tomography
4R	4 repeat
AB42	Amyloid beta 42
AD	Alzheimer's disease
ANLS	Astrocyte-Neuron Lactate Shuttle
ATP	Adenosine Triphosphate
CBD	Corticobasal degeneration
CBS	Corticobasal syndrome
CMRglc	Cerebral metabolic rate of glucose
CSF	Cerebrospinal fluid
DWI	Diffusion weighted imaging
FDR	False discovery rate
FTLD	Frontotemporal lobar degeneration
FWE	Family-wise error
FWHM	Full-width at half-maximum
GLM	General linear model
GM	Grey matter
HRRT	High resolution research tomograph
MFG	Middle frontal gyrus
ML	Machine learning
MMSE	Mini mental state examination
MNI	Montreal Neurological Institute
MRI	Magnetic resonance imaging
PVC	Partial volume correction
PVE	Partial volume effects
rCMRglc	Regional cerebral metabolism rate of glucose
SFG	Superior frontal gyrus

SMA	Supplementary motor area
TAC	Time activity curve
UPDRS	Unified Parkinson's Disease Rating Scale
VOI	Volume of interest
WM	White matter

## List of Figures

<b>Figure 1</b> Processing Steps.....	28
<b>Figure 2</b> Grey Matter, White Matter and Cerebrospinal Fluid Tissue Probability Map ...	30
<b>Figure 3</b> Regions defined via the Hammersmith Probability Atlas .....	30
<b>Figure 4</b> Compartmental Model of FDG and Glucose Kinetics .....	31
<b>Figure 5</b> Parametric CMRglc Map ( $\mu\text{mol}/\text{ml}/\text{min}$ ) and T1-MRI from a CBS-AD patient ..	32
<b>Figure 6</b> Weighted Average Calculation of the Parietal Lobe.....	33
<b>Figure 7</b> Atlas-defined VOIs Displayed on Co-registered MR-to-PET Images .....	34
<b>Figure 8</b> Parametric CMRglc Maps in Controls, CBS-CBD and CBS-AD patients .....	37
<b>Figure 9</b> rCMRglc in Controls and CBS Subgroups: Mann-Whitney U Test Results .....	41
<b>Figure 10</b> Montage of Voxel-wise Hypometabolism in Patients Relative to Controls ....	43

## List of Tables

<b>Table 1</b> Apraxia Domains and Manifestation in CBS Pathologies .....	19
<b>Table 2</b> Patient Demographics and Clinical Data .....	26
<b>Table 3</b> VOIs Defined via the Hammersmith Probabilistic Atlas .....	34
<b>Table 4</b> Percentage Difference in Median rCMRglc (controls – patients).....	39
<b>Table 5</b> Percentage Difference in Median rCMRglc (CBS-AD – CBS-CD).....	40
<b>Table 6</b> Peak Voxel-wise Hypometabolism in Patients Relative to Controls .....	42

## Abstract

Corticobasal syndrome (CBS) is a clinically heterogeneous syndrome with multiple underlying pathologies, most notable corticobasal degeneration (CBD) and Alzheimer's disease (AD). Accurate *in vivo* diagnosis of the underlying pathology is clinically challenging, with overlapping symptom profiles leading to misdiagnosis. [<sup>18</sup>F]FDG-PET provides a sensitive measure of glucose metabolism, which may provide pathology-specific biomarkers to improve diagnostic accuracy.

The study investigates glucose metabolism patterns across controls and CBS patients (CBD and AD) using [<sup>18</sup>F]FDG-PET. Complementary volume of interest and voxel-wise analysis of quantitative cerebral metabolic rate of glucose metabolism maps was conducted across 10 controls and 12 patients (7 CBS-CBD, 5 CBS-AD).

Compared to controls, CBS patients showed widespread cortical and subcortical hypometabolism, most prominently in the precentral gyrus ( $p < .001$ ; -29% change), middle frontal gyrus ( $p < .001$ ; -12% change) and caudate nucleus ( $p < .001$ ; -33% change). Both CBS-AD and CBS-CBD groups showed marked frontal hypometabolism, volume of interest analysis revealed additional hypometabolism in the posterior temporal gyrus ( $p = .030$ ; -19% change) and parietal lobe ( $p = .048$ ; -26% change) in CBS-AD relative to CBS-CBD. CBS-CBD patients showed relative sparing of temporoparietal regions. Voxel-wise analysis confirmed patient-control differences in frontoparietal cortices, but did not detect any significant subgroup distinctions, underscoring the subtle differences between pathologies.

These findings support FDG-PET metabolism as a valuable tool for identifying pathology-specific metabolism patterns. Distinct patterns of temporoparietal versus frontostriatal hypometabolism may aid in differentiating underlying pathologies, while shared motor network dysfunction provides an explanation for similar clinical phenotypes. Together, these results highlight the potential for FDG-PET to provide a reliable imaging marker of CBS pathology.

## **Declaration**

No portion of the work referred to in the dissertation has been submitted in support of an application for another degree or qualification of this or any other university or other institute of learning.

## Intellectual Property Statement

- i. The author of this dissertation (including any appendices and/or schedules to this dissertation) owns certain copyright or related rights in it (the "Copyright") and s/he has given The University of Manchester certain rights to use such Copyright, including for administrative purposes.
- ii. Copies of this dissertation, either in full or in extracts and whether in hard or electronic copy, may be made only in accordance with the Copyright, Designs and Patents Act 1988 (as amended) and regulations issued under it or, where appropriate, in accordance with licensing agreements which the University has entered into. This page must form part of any such copies made.
- iii. The ownership of certain Copyright, patents, designs, trademarks and other intellectual property (the "Intellectual Property") and any reproductions of copyright works in the dissertation, for example graphs and tables ("Reproductions"), which may be described in this dissertation, may not be owned by the author and may be owned by third parties. Such Intellectual Property and Reproductions cannot and must not be made available for use without the prior written permission of the owner(s) of the relevant Intellectual Property and/or Reproductions.
- iv. Further information on the conditions under which disclosure, publication and commercialisation of this dissertation, the Copyright and any Intellectual Property and/or Reproductions described in it may take place is available in the University IP Policy, in any relevant Dissertation restriction declarations deposited in the University Library, and The University Library's regulations.

## Acknowledgements

I would like to thank Dr Rainer Hinz and Dr Tobias Langheinrich for their invaluable guidance and support throughout this project. This advice has been instrumental in shaping the study. I would like to thank Professor Karl Herholz for his insightful input in interpreting unexpected findings.

Finally, I wish to thank the staff at the Wolfson Molecular Imaging Centre for their assistance and providing an excellent research environment that made this study possible.

## 1. Literature Review

### 1.1 Principles of Cerebral Glucose Metabolism in FDG-PET

#### 1.1.1 Glucose transport and utilisation

Glucose is the primary energy substrate in the brain. It is transported across the blood-brain barrier via high-affinity glucose transporters: GLUT1 in endothelial cells and GLUT3 in neurons (Herholz et al., 2004; Pauwels, 2001; Maher, 1995). Once inside the cell, glucose undergoes a series of metabolic processes. Initially, it undergoes glycolysis and is phosphorylated by the enzyme hexokinase to produce glucose-6-phosphate. The pyruvate produced from this process is then oxidised in the tricarboxylic acid cycle, leading to the production of adenosine triphosphate (ATP). Glucose-6-phosphate also enters the pentose phosphate pathway, contributing to the synthesis of nicotinamide adenine dinucleotide phosphate synthesis (Pauwels, 2001). Together, these pathways contribute to the metabolism of glucose, supporting neuronal activity.

Glucose metabolism is predominantly driven by synaptic activity, as myelinated axons allow energy-efficient axonal conduction (Harris et al., 2012; Magistretti & Allaman, 2015). Synaptic transmission imposes high energy demands, and its metabolic support is mediated by astrocytes. Pellerin and Magistretti (1994) formalised this process in the Astrocyte-Neuron Lactate Shuttle (ANLS), in which astrocytes take up glucose, and in response to increased synaptic activity, stimulate glycolysis. This produces lactate, which is in turn used to generate ATP. The ANLS model underscores the role of astrocytes as key intermediaries, connecting synaptic activity to regional energy metabolism.

While the ANLS provides a solid framework for understanding astrocytic function, its validity is debated. Alternative perspectives suggest that neurons can directly uptake glucose to sustain synaptic transmission, raising doubt over whether lactate shuttling is a primary or complementary pathway (Dienel, 2012). This highlights the complexity of cellular energy metabolism and cautions against simplistic interpretations of glucose utilisation as a reflection of astrocytic-neuronal coupling, regardless, synaptic activity is the primary driver of glucose utilisation. Regional variations in glucose metabolism

can be measured using Fluorine-18 fluorodeoxyglucose Positron Emission Tomography ( $[^{18}\text{F}]\text{FDG-PET}$ ), providing a measure of neural activity.

### 1.1.2 $[^{18}\text{F}]\text{FDG}$ uptake and PET quantification

PET is an imaging technique that quantifies physiological and metabolic processes *in vivo*, including cerebral glucose metabolism, commonly used with the radiotracer  $[^{18}\text{F}]\text{FDG}$ . Due to their similar chemical composition,  $[^{18}\text{F}]\text{FDG}$  is a glucose analogue except it contains an  $^{18}\text{F}$  atom at the second carbon rather than a hydroxyl group. This difference allows  $[^{18}\text{F}]\text{FDG}$  to enter glycolysis and be phosphorylated to FDG-6-phosphate but prevents any further metabolism. As a result,  $[^{18}\text{F}]\text{FDG}$  becomes metabolically trapped within the cell and decays, making its accumulation proportional to local glucose uptake (Pauwels, 2001; Sokoloff et al., 1977).

Following positron decay,  $^{18}\text{F}$  emits two 511keV photons. The PET scanner detects these coincidences, allowing three-dimensional tomographic reconstruction of regional  $[^{18}\text{F}]\text{FDG}$  (Valk et al., 2002). Uptake is highest in grey matter (GM), reflecting the high density of synapses, with cerebral metabolic rate of glucose (CMR<sub>glc</sub>) values typically ranging from  $0.40\text{--}0.60 \mu\text{mol ml}^{-1} \text{ min}^{-1}$  in GM, compared to  $0.15 \mu\text{mol ml}^{-1} \text{ min}^{-1}$  in white matter (WM; Herholz et al., 2004; Magistretti & Allaman, 2015). Thus,  $[^{18}\text{F}]\text{FDG-PET}$  is a reliable proxy for local metabolic demand and, by extension, neural activity. The signal represents a cumulative measure of glucose metabolism over the uptake period, making  $[^{18}\text{F}]\text{FDG-PET}$  sensitive to region-specific metabolic dysfunction in neurodegenerative diseases.

### 1.1.3 FDG-PET limitations and image analysis approaches

Despite  $[^{18}\text{F}]\text{FDG-PET}$ 's advantage of being an intrinsically quantitative measure (Soret et al., 2007), it has several technical and methodological limitations, especially in neurodegenerative disorders with severe atrophy. One of the most significant limitations is the presence of partial volume effects (PVEs), which can distort the intensity values in PET images. Two distinct phenomenon give rise to PVEs, introducing systematic bias to the data PVEs (Thomas et al., 2011; Soret et al., 2007).

One cause of PVE is the finite resolution effect, which results from the limited spatial resolution of PET scanners, typically 2-3 mm full-width at half-maximum (FWHM; de Jong et al., 2007). Due to this, three-dimensional blurring occurs. Signals from metabolically active regions can "spill out" into neighbouring areas, causing an underestimation of activity in the original region, and surrounding tissue signals can also "spill in" and artificially inflate apparent activity in the region of interest (Thomas et al., 2011; Soret et al., 2007). In corticobasal syndrome (CBS), asymmetrical atrophy leads to irregular tissue boundaries, which further exacerbate the prevalence of spillover effects (Albrecht et al., 2017). Together, these spillover effects compromise the accuracy of regional measurements and reduce the anatomical specificity of PET data.

Tissue fraction effects also cause PVEs (Thomas et al., 2011; Soret et al., 2007). As PET images are sampled using a voxel grid, a mismatch arises between this grid and the continuous nature of anatomical structures in the brain. A single voxel may contain multiple tissue types, with the metabolic measurements reflecting the average of these tissue types rather than the true activity of the volume of interest. The degree of tissue fraction effects is influenced by the size of the structure, making them particularly pronounced in neurodegenerative disorders with severe atrophy (Thomas et al., 2011). For example, there may be an increase in the proportion of non-GM (i.e., cerebrospinal fluid; CSF) in the voxel, diluting the metabolic signal. Schmidt et al. (1991, 1992) demonstrated that tissue heterogeneity within PET voxels systematically biases kinetic modelling of [<sup>18</sup>F]FDG uptake. Conventional compartmental models can overestimate CMRglc, especially apparent dephosphorylation, meaning values reflect the heterogeneity of tissue rather than glucose utilisation. These findings highlight that PVEs not only degrade spatial accuracy but also propagate through kinetic analysis, compounding quantification errors in atrophied brains.

Several partial volume correction (PVC) techniques have been proposed to address PVEs, including the Meltzer method, which is region-based (Meltzer et al., 1990) and the Müller-Gärtner approach, which is voxel-based (Müller-Gärtner, 1992). These methods attempt to compensate for PVEs, however, their application is limited in neurodegenerative populations (Thomas et al., 2011). They rely on accurate

segmentation and co-registration between PET and magnetic resonance imaging (MRI) images, but severe atrophy in neurodegeneration increases the risk of errors in these processing steps (Rousset et al., 1998; Shidahara et al., 2017). Due to this high sensitivity to image processing errors, caution is needed when applying PVCs to patient groups.

Additional challenges arise when linking cellular models of glucose metabolism to [<sup>18</sup>F]FDG-PET findings. The ANLS model (Pellerin & Magistretti, 1994) suggests that astrocytes mediate the link between synaptic activity and glucose metabolism. By taking [<sup>18</sup>F]FDG-PET measures as an indirect measure of neuronal function, this assumes intact neuro-glial coupling, which may not be the case in neurodegenerative populations. For example, in CBS-corticobasal degeneration (CBD), astrocytic plaques impair astrocytic function, decoupling synaptic demand from glucose utilisation and disrupting the ANLS (Aiba et al., 2023). Moreover, [<sup>18</sup>F]FDG uptake is not unique to neurons; astrocytes and other glial cells also contribute to the PET signal (Zimmer et al., 2017). Consequently, reductions in [<sup>18</sup>F]FDG uptake may reflect altered glial function, or impaired astrocyte-neuron communication, rather than synaptic dysfunction alone. This complexity complicates the interpretation of hypometabolism in neurodegenerative populations.

Volume of interest (VOI) analysis of PET data is a hypothesis-driven approach that extracts data from predefined volumes, guided by standardised brain atlases such as the Hammersmith Probabilistic Atlas (Hammers et al., 2003). This method benefits from improved signal-to-noise by averaging the signal across predefined volumes, reducing voxel-level variance and improving signal reliability (Greve et al., 2014). However, this comes at the expense of anatomical precision, as the low spatial resolution of PET and PVEs can blur anatomical boundaries; therefore, atlas-based methods may not accurately reflect the true metabolic distribution in atrophied regions (Thomas et al., 2011; Soret et al., 2007). Furthermore, as this approach is driven by a priori assumptions, it may overlook unexpected abnormalities outside the predefined regions.

Voxel-wise analysis provides a solution to this by conducting a statistical comparison across the entire brain, rather than predefined volumes (Ashburner & Friston, 2000). This enables data-driven localisation of metabolic effects, allowing the detection of any unexpected patterns of hypometabolism. Voxel-wise analysis is also more robust to the effects of atrophy; it utilises nonlinear registration algorithms that can deform asymmetrical brains into standard space, reducing misalignment (Senjem et al., 2009). However, as analysis is conducted at the voxel level, there is increased noise in the data which reduces statistical power, therefore, spatial smoothing is required to compensate for this (Greve et al., 2014). As comparison is conducted across the entire brain, there is also an increased risk of type I error. Given the relative strengths and weaknesses of voxel-wise comparison and VOI, a complementary use of the two approaches is beneficial. VOI analysis can provide clear, anatomically interpretable results, while voxel-wise comparison offers a sensitive, unbiased exploratory approach for identifying unexpected patterns of hypometabolism.

## 1.2 CBS and underlying pathologies

CBS is a rare neurodegenerative movement disorder, affecting approximately 0.6-0.9 per 100,000 individuals, with a mean age of onset of 64 years (Armstrong et al., 2013; Constantinides et al., 2019). It involves dysfunction in both cortical and basal ganglionic regions (Peigneus et al., 2001). However, CBS is not a unitary disease. It is a clinically syndrome that can reflect several underlying pathologies, including CBD, Alzheimer's disease (AD), progressive supranuclear palsy (PSP), frontotemporal lobar degeneration (FTLD), and dementia with Lewy bodies (DLB) (Constantinides et al., 2019; Shir et al., 2023). The present paper will focus on CBS-CBD and CBS-AD.

### 1.2.1 Clinical Heterogeneity and Diagnostic Challenges

The clinical heterogeneity across CBS pathologies presents significant diagnostic challenges. A hallmark feature across CBS is asymmetrical presentation, reflecting underlying lateralised neurodegeneration (Armstrong et al., 2013). Clinically, this manifests as unilateral rigidity, bradykinesia, dystonia, and apraxia. This asymmetry is evident in structural imaging studies. MRI reveals atrophy of GM in the frontoparietal

cortex contralateral to the more affected limb, as well as WM atrophy in the contralateral premotor and motor cortices (Shir et al., 2023).

Some symptoms allude to the underlying pathology. For example, alien limb syndrome and frozen gait are suggestive of CBS-CBD, while early speech or cognitive impairment indicates CBS-AD (Aiba et al., 2023). However, symptom profiles tend to show high overlap, complicating *in vivo* diagnosis. A retrospective study from Aiba et al. (2023) found that only 33% of patients initially diagnosed with CBS were confirmed to have CBS-CBD at autopsy, with 12.5% diagnosed as CBS-AD. Such data can be difficult to interpret due to the temporal disconnect between clinical diagnosis and post-mortem confirmation. While the underlying proteinopathy remains stable, clinical features evolve over time and co-pathologies may emerge, obscuring clinicopathological correlations (Aiba et al., 2023). Consequently, retrospective diagnostic markers may not accurately reflect the full disease course.

Misdiagnosis of CBS has significant treatment implications. CBS-AD patients often benefit from acetylcholinesterase inhibitors, while cognitive interventions are avoided (NICE, 2018). In contrast, no effective pharmacological intervention has been identified for CBS-CBD, so management takes a symptomatic approach guided by treatments used in related conditions (Caixeta et al., 2020). For example, CBS-CBD patients tend to show a more rapid decline in story recall and verbal fluency (Day et al., 2017), so a timely and accurate diagnosis is essential to optimise treatment plans as early as possible.

A core clinical feature of CBS is apraxia, characterised by patient difficulty in executing movements. Crucially, apraxia is not a loss of motor control but rather reflects impairments in the cognitive organisation of action (Goldenberg, 2013, 2016). Traditionally, literature refers to apraxia presentation as either ideomotor (difficulty performing purposeful movements; Buxbaum, 2001) or imitation (difficulty copying gestures; Goldenberg, 1999). These classifications are grounded in a two-part system of praxia mediation proposed by Roy and Square (1985). Recently, Goldenberg (2013, 2016) has argued that these classifications are unclear, proposing a revised four-domain classification based upon cognitive processes and their neural correlates,

presented in Table 1. While apraxia can manifest in many forms across CBS pathologies, its presentation provides limited diagnostic insight.

**Table 1***Apraxia Domains and Manifestation in CBS Pathologies*

Domain	Cognitive Basis	Neural Correlates	Manifestation in CBS-AD	Manifestation in CBS-CBD
Imitation of Gesture	Body-part coding, visuo-spatial analysis	Left parietal lobe, frontal/subcortical regions	Impaired in meaningless and meaningful imitation	Severely impaired meaningless gestures
Communicative Gestures	Semantic knowledge of culturally learned gestures	Left inferior frontal and temporal cortices, parietotemporal junction (angular and supramarginal gyrus)	Disrupted	Relatively spared due to temporal preservation
Tool use (single object)	Functional knowledge (semantics) and mechanical problem solving	Frontal-temporal semantic systems (functional); parietal circuits (mechanical reasoning)	Errors in functional knowledge and pantomime use of tools	Severe impairment of mechanical reasoning but functional knowledge spared
Multistep actions	Sequencing and sustained attention across action chains	Left hemisphere (semantic/ scripts retrieval); right hemisphere (attentional control/ neglect)	Frequent slips of action	Errors linked to attentional deficits

Note. Adapted from Goldenberg (2013, 2016).

To address the diagnostic challenges and improve accuracy, Armstrong et al. (2013) proposed a diagnostic criterion for CBS-CBD based upon expert consensus, analysis of brain bank data, and an extensive literature review. Two diagnostic criteria were identified: probable and possible CBD. Probable CBD aims to capture classic cases with higher specificity, requiring onset after age 50 and no family history or known tau mutations. The possible CBD criteria is broader, allowing for a wider range of presentation but with a higher risk of false positives. However, the predictive value of the Armstrong criteria remains modest, with only 40-60% of clinically defined cases confirmed as CBD at autopsy (Shir et al., 2023). Supporting this concern, Alexander et al. (2014) found that this criterion failed to identify a third of CBD cases, showing low diagnostic accuracy persists.

Building on this criterion, advancements in biomarkers have improved CBS diagnosis. CSF biomarkers, such as tau protein and amyloid beta 42 (A $\beta$ 42), can help discriminate between underlying pathologies (Constantinides et al., 2019). Low A $\beta$ 42 (<500 pg/mL) and high tau (>300 pg/mL) predict CBS-AD with 90% accuracy (Tapiola et al., 2009). In contrast, CBS-nonAD patients typically show normal levels of these proteins, aiding in the identification of Alzheimer's pathology (Constantinides et al., 2019). Caution is required when interpreting amyloid-positive CSF, however, as half of cognitively normal individuals have amyloid-positive CSF at age 90 (Jansen et al., 2015). Thus, positive amyloid markers may reflect an incidental co-pathology rather than the primary cause of symptoms.

Alongside CSF biomarkers, neuroimaging biomarkers, such as [ $^{18}\text{F}$ ]PI-2620 tau-PET, have also shown enhanced specificity for 4-repeat (4R) tauopathies. Neurofilament light chain can also indicate non-AD pathology, but these markers of axonal injury lack disease specificity (Khalil et al., 2018). The specificity of these markers to differentiate between tau pathologies remains limited, but advances represent a significant shift in diagnostic accuracy, facilitating therapeutic trials for CBS (Malarte et al., 2023).

### 1.2.2 Neuropathology of CBD and AD

Currently, the underlying pathology of CBS is confirmed postmortem.

Neuropathologically, CBS-CBD is characterised by the deposition of

hyperphosphorylated 4R-tau in neurons and glial cells. This is accompanied by significant neuronal loss, astrocytic plaques, and ballooned neurons (Armstrong et al., 2013). Astrocytic plaques represent a pathognomonic feature of CBD; they appear as tau-positive brush-like inclusions in astrocytic processes (Feany & Dickson, 1995). On the other hand, hyperphosphorylated 4R-tau is observed across various pathologies such as CBS-PSP. However, CBS-PSP tends to demonstrate distinct midbrain atrophy patterns, particularly in the superior colliculus and substantia nigra, as well as pronounced neuronal loss in subcortical structures (Aiba et al., 2023; Armstrong et al., 2013).

Although clinically overlapping with CBS-CBD, CBS-AD presents a distinct set of neuropathological features. It is characterised by extracellular A $\beta$  plaques and intracellular neurofibrillary tangles comprising hyperphosphorylated tau, which predominantly affect the posterior temporoparietal regions of the brain (Constantinides et al., 2019). This spatial distribution contrasts with CBS-CBD pathology, which primarily involves the frontal-parietal cortex and basal ganglia regions (Constantinides et al., 2019). CBS-AD can further be discriminated from CBS-CBD by intact WM structures, which typically show marked myelin pallor and gliosis in CBS-CBD (Feany & Dickson, 1995).

Given the distinct pathological signature and advances in CSF biomarkers, the diagnosis of CBS-AD has significantly improved. However, biomarkers are not as accurate for distinguishing between non-AD pathologies (Ossenkoppele et al., 2021). Diagnostic accuracy is further undermined by the increasing prevalence of co-pathologies with age. This increases the risk of misdiagnosis and highlights the urgent need for enhanced pathological differentiation.

### 1.2.3 Neuroimaging signatures of CBS pathologies

While some imaging features are consistent across CBS pathologies, others show specificity that may help to differentiate them. Structural MRI studies consistently demonstrate GM atrophy in the insula, premotor cortex, and caudate nucleus across CBS patients (Whitwell et al., 2010). However, in CBS-CBD, GM volume loss is typically observed in the frontoparietal cortices, specifically in the premotor cortex and

supplementary motor area (SMA). Subcortical structures, including the basal ganglia and putamen, are also affected (Boxer et al., 2006). The superior frontal gyrus (SFG) is also a prominent site of atrophy in CBS-CBD, aligning with postmortem reports of a high density of ballooned neurons in this region (Boxer et al., 2006; Dickson et al., 2002). In contrast, CBS-AD patients tend to show relative sparing of frontal regions, with more pronounced atrophy in the temporoparietal cortices, specifically the precuneus and posterior lateral temporal lobe (Whitwell et al., 2010).

Functional imaging further highlights the metabolic profiles associated with different CBS pathologies. In CBS-CBD, studies have consistently reported asymmetric hypometabolism contralateral to the affected limb, particularly in the premotor cortex, SMA, and basal ganglia (Pardini et al., 2019; Shir et al., 2023). CBS-AD patients typically show hypometabolism in temporoparietal regions as well as ipsilateral hypometabolism of the supramarginal gyrus and superior parietal lobe, similar to the imaging profile of typical AD (Constantinides et al., 2019; Pardini et al., 2019; Whitwell et al., 2010).

Imaging findings have also revealed how specific clinical features, such as apraxia, map onto regional metabolism dysfunction. Peigneux et al (2001) demonstrated that apraxic CBS-CBD patients show hypometabolism in the superior parietal lobule, medial and middle frontal gyrus (MFG), and anterior cingulate cortex, regions associated with integrating sensory information into coordinating action. Notably, these metabolic deficits persisted even after accounting for GM atrophy. This suggests they reflect true dysfunction, rather than structural loss alone. When the authors defined apraxia more stringently (based on the patient's ability to correct errors), hypometabolism was observed in the contralateral superior parietal lobule, the SMA, and the MFG, and ipsilaterally in the precentral gyrus and the superior parietal lobule. These regions are involved in transforming perceptual representations into motor outputs, aligning closely with the innervatory pattern stage of Gonzalez Rothi et al.'s (1991) model of praxis. Furthermore, Peigneux et al. (2001) found no hypometabolism in the occipitotemporal junction, which is involved in visuo-gestural analysis. This consolidates the idea that apraxia is caused by deficits in transforming perceptual information into motor outputs, rather than being the result of early perceptual

deficits. These findings reinforce the notion that apraxia in CBS reflects a breakdown in higher-order sensorimotor integration rather than basic perceptual processing. FDG-PET can sensitively capture the functional disconnections underlying these deficits, providing insights beyond structural imaging.

Subsequent work has suggested that apraxia subtypes may correspond to distinct metabolic signatures. Jo et al. (2021) reported that both imitation and ideomotor apraxia are correlated with contralateral frontoparietal hypometabolism. However, imitation apraxia was additionally linked to hypometabolism in the posterior cingulate and precuneus (areas more typically associated with AD), and ideomotor apraxia was associated with reduced metabolism in the angular gyrus. These findings suggest the possible anatomical dissociation of apraxia subtypes; however, the diagnostic specificity is limited given the absence of pathological confirmation in the cohort.

Pathologically confirmed studies reinforce this concern. Pardini et al. (2019) demonstrated that apraxia severity correlated with hypometabolism in the SFG and MFG and the precentral gyrus, regardless of underlying pathology. Such convergence suggests that frontoparietal dysfunction represents a shared substrate of praxis breakdown across CBS, limiting its value as a differential biomarker. Moreover, FDG uptake cannot be assumed to reflect neuronal dysfunction alone, since astrocytic function can also contribute to the PET signal (Zimmer et al., 2017). These findings suggest that apraxia reflects a network-level vulnerability common to multiple proteinopathies, and caution should be applied when interpreting FDG-PET correlates as pathology-specific markers of apraxia.

Although neuroimaging has advanced our understanding of CBS, the clinical utility for individual diagnosis remains limited. Given the low predictive value of current diagnostic criteria (Shir et al., 2023), efforts are needed to better differentiate the underlying pathologies of CBS. CSF biomarkers have shown high sensitivity to AD pathology, however, their ability to differentiate non-AD pathologies remains limited (Constantinides et al., 2019). FDG-PET, in contrast, provides network-level topographical information regarding regional dysfunction. This offers the potential to characterise frontostriatal involvement of CBS-CBD and posterior temporoparietal

involvement in CBS-AD. FDG-PET therefore offers a potential imaging marker to differentiate CBS pathologies, beyond what CSF biomarkers offer. However, FDG-PET data remains constrained by its limited spatial resolution, PVEs, and variability in image acquisition and processing pipelines (Thomas et al., 2011; Shidahara et al., 2017).

### 1.3 Aims and hypotheses

Previous literature has highlighted the clinical overlap and pathological heterogeneity of CBS, with some pathology-specific differences. CBS-CBD is typically characterised by hypometabolism in frontal regions and the basal ganglia, while CBS-AD is associated with temporoparietal hypometabolism (Pardini et al., 2019; Shir et al., 2023). However, there is substantial neural overlap between the two groups, even in autopsy-confirmed cases (Pardini et al., 2019).

To address the diagnostic uncertainty surrounding CBS, this study aims to distinguish FDG-PET patterns of glucose metabolism in CBS cases compared to healthy controls, and to further distinguish the metabolic profiles of CBS-CBD and CBS-AD. By employing complementary VOI and voxel-wise analysis, the study offsets the inherent limitations of both approaches, providing more reliable pathology-specific patterns of metabolism for diagnosis.

Hypothesis:

1. CBS patients will show asymmetrical hypometabolism, with reductions localised to frontoparietal and subcortical regions compared to controls.
2. Within the patient group:
  - a. CBS-CBD patients will show greater hypometabolism in motor and frontal regions (precentral gyrus, SFG, MFG, anterior cingulate cortex) and subcortical structures (putamen, pallidum, thalamus, and caudate nucleus), relative to CBS-AD.
  - b. CBS-AD patients will demonstrate significant hypometabolism in the temporoparietal regions (posterior temporal gyrus, inferior parietal lobule) and the hippocampus, relative to CBS-CBD.

## 2. Methods

Data were acquired from an unpublished study conducted at the University of Manchester. PET frames had undergone prior frame-to-frame realignment and resolution-modelling image reconstruction.

### 2.1 Participants

Twelve patients were recruited from specialist neurology clinics at the Greater Manchester Neuroscience Centre, including the Cerebral Function Unit and the Movement Disorder Clinic. All patients were diagnosed with either CBS-AD ( $n = 5$ ) according to the International Working Group-2 criteria for atypical AD (Dubois et al., 2014) or CBS-CBD ( $n = 7$ ) as per Boeve et al. (2003). Demographic and clinical data on all patients are presented in Table 2.

Ten healthy age-matched controls (60-76 years) were extracted from Carter et al. (2014). All controls were neurologically healthy with no history of cognitive or motor impairment.

### 2.2 Clinical and Neuropsychological Assessments

All patients underwent a full neurological examination. Testing included the motor subsection of the Unified Parkinson's Disease Rating Scale (UPDRS), with a higher score indicating greater impairment (Fahn et al., 1987). They were also assessed using a comprehensive neuropsychological battery covering several cognitive domains: language (comprehension, repetition, reading, writing), perception (object and face recognition, degraded stimulus interpretation), spatial skills (localisation, spatial judgement, 3D appreciation), working and episodic memory, and executive function (abstraction, sequencing, verbal fluency). Patients also completed the Mini-Mental State Exam (MMSE), scored out of 30, with a score below 24 indicating cognitive impairment (Folstein et al., 1975).

Patient apraxia was assessed using a battery developed by Luzzi et al. (2008), which included comprehension tasks (e.g., gesture identification, object-function matching, and body part tool use matching) and representational tasks (e.g., pantomime and imitation of symbolic gestures, single- and multi-object use). All responses were

videotaped and subsequently coded for error type and scored on parameters including timing, amplitude, sequencing, spatial configuration, and action content. Apraxia was classified based on Goldenberg's (2016, 2024) classification, as either motor (failures copying to command and imitation) or spatial (failures copying to imitation).

Control participants completed a range of neuropsychological tests to establish normal cognitive function. This included assessment of global cognition, episodic and semantic memory, language, and executive/ attention tests (Carter et al., 2012).

**Table 2**

*Patient Demographics and Clinical Data*

Participant	Diagnosis	Age	MMSE	UPDRS	Apraxia subtype	Apraxia side
h00557	CBS-AD	69	20	42	Spatial	Right
h00559	CBS-CBD	62	25	22	Motor	Right
h00558	CBS-AD	59	15	39	Spatial	Right
h00803	CBS-CBD	64	28	15	Motor	Right
h00828	CBS-AD	53	12	2	Spatial	Left
h00865	CBS-CBD	80	23/28	43	Motor	Right
h00885	CBS-CBD	76	25/28	44	Motor	Right
h01006	CBS-CBD	80		60	Motor	Left
h01042	CBS-AD	63	12	18	Spatial	Left
h01043	CBS-CBD	62	28	6	Motor	Left
h01044	CBS-CBD	62	22	54	Both	Right
h01115	CBS-AD	65	18	17	Spatial	Left

Note. Participants h0065 and h00885 were unable to use a pen, so they could only answer 28/30 questions on the MMSE. No MMSE data was available for patient h01006.

## 2.3 Imaging Acquisition

### 2.3.1 FDG-PET

All PET scans were performed on a High-Resolution Research Tomograph (HRRT, Siemens/CTI) at the Wolfson Molecular Imaging Centre. Participants received a slow intravenous bolus injection of 370 MBq [<sup>18</sup>F]FDG. Dynamic acquisition commenced immediately and continued for 60 minutes, capturing tracer uptake during the

established linear phase of cerebral glucose metabolism. Full 60-minute dynamic images and plasma input functions were used to calculate CMRglc with spectral analysis. Participants were scanned in resting state (with eyes closed in a supine position) to minimise variability from task-related neural activity.

### 2.3.2 Structural MRI

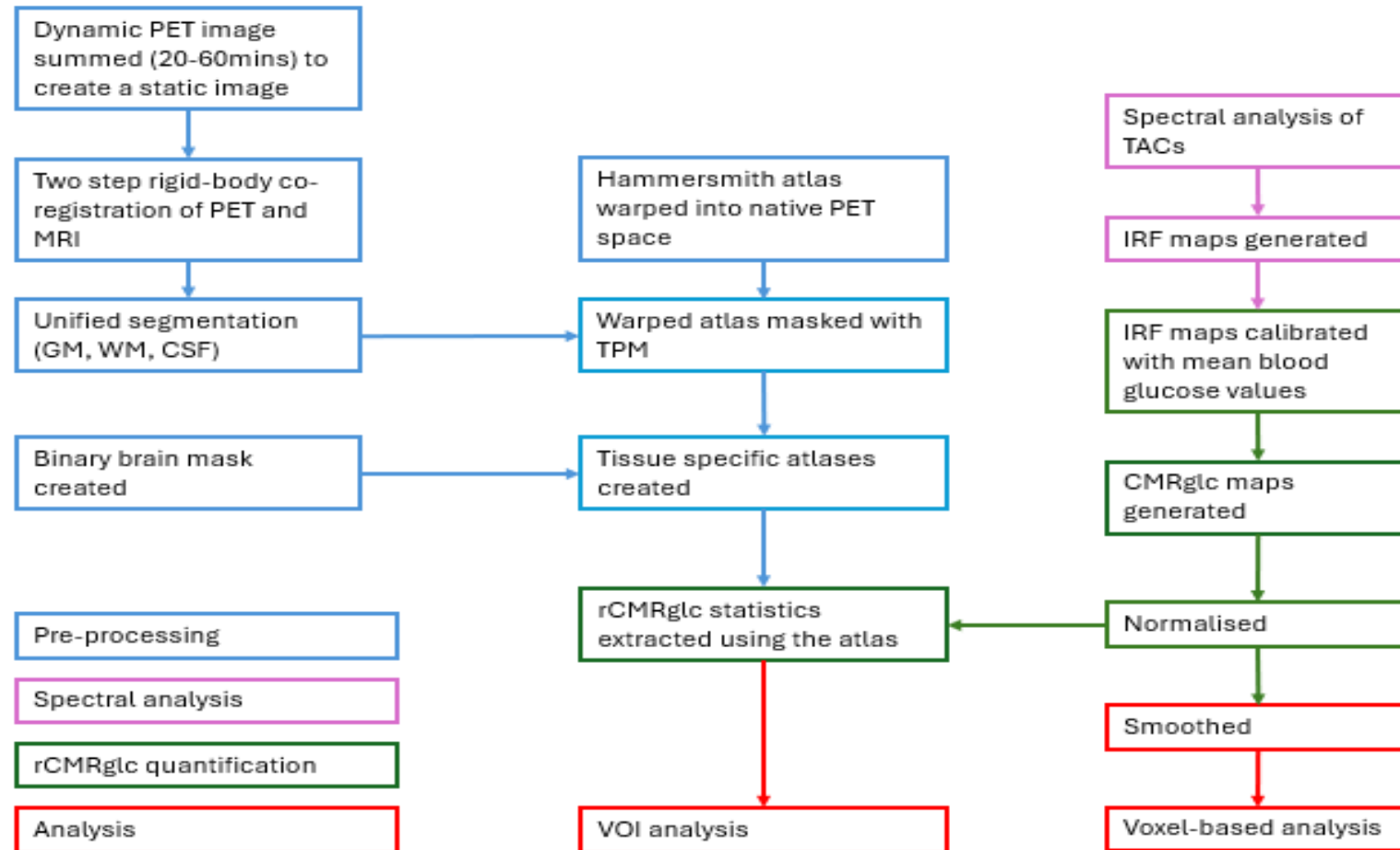
Structural T1-weighted MR images were acquired using a 3 Tesla Philips Achieva scanner with an 8-channel Sensitivity Encoding Spin Echo head coil. A T1-weighted inversion recovery acquisition was acquired parallel to the anterior/ posterior commissure line with a 3D acquisition. MRI data were used for co-registration and segmentation.

## 2.4 Image Analysis

All data were processed in a Linux system using FSL (v6.0.6.4; Jenkinson et al., 2012), Analyze 11.0 (Robb & Hanson, 1991), and SPM12 (Wellcome Trust Centre for Neuroimaging, 2012) implemented in MATLAB R2024a (The MathWorks Inc., 2024). See Figure 1 for the processing pipeline.

**Figure 1**

*Processing Steps*



Note. GM: grey matter, WM: white matter, CSF: cerebrospinal fluid, TPM: tissue probability map, TACs: time activity curves, IRF: impulse response function, rCMRglc: regional cerebral metabolism rate of glucose.

#### 2.4.1 Pre-processing

Each participant's PET and MRI images were co-registered using a two-step process in FSL. Dynamic PET frames from 20-60 minutes post-injection were summed to produce a static image. Rigid-body co-registration was applied to the static PET image, aligning it with the corresponding T1-weighted MRI using six degrees of freedom, preserving the voxel dimensions. The resulting transformation matrix was inverted and used to resample the MRI into native PET space, retaining PET spatial resolution while incorporating anatomical information from the structural MR image. Visual inspection of the accuracy of this process revealed it had failed in one participant, so direct MRI-to-PET alignment was applied.

Binary brain masks were created from the static PET image using the object extractor tool in Analyze. This was completed manually to ensure inclusion of atrophied regions, which may be misclassified by automated tools. Masks were refined via morphological dilation and hole filling. Final masks were visually inspected to verify mask coverage and brain edge conformity.

Tissue segmentation of the co-registered image was performed using SPM12's unified segmentation framework (Ashburner & Friston, 2005), generating GM, WM, and CSF probability maps (Figure 2). Segmentation outputs were generated in native space. Forward and inverse deformation fields were generated for each subject, representing transformations between native and Montreal Neurological Institute (MNI) space.

The inverse deformation fields were applied to the Hammers Probabilistic Atlas (Figure 3; Hammers et al., 2003) to warp it to each subject's native PET space using nearest-neighbour interpolation. GM and WM-specific atlases were then derived by masking the warped probabilistic atlas with tissue probability maps (TPM; thresholded at 80%), enhancing the anatomical specificity of region labels.

**Figure 2**

## *Grey Matter, White Matter, and Cerebrospinal Fluid Tissue Probability Map*

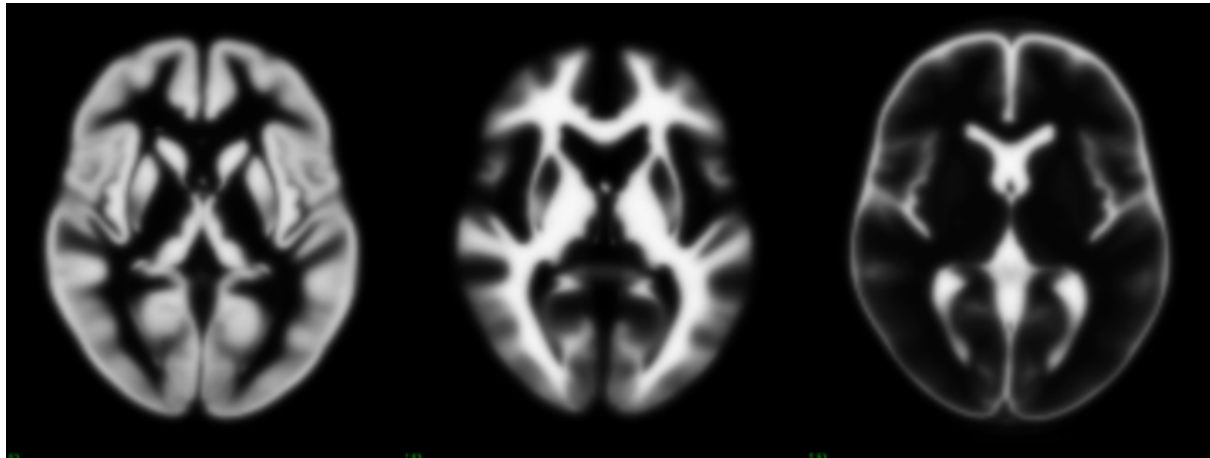
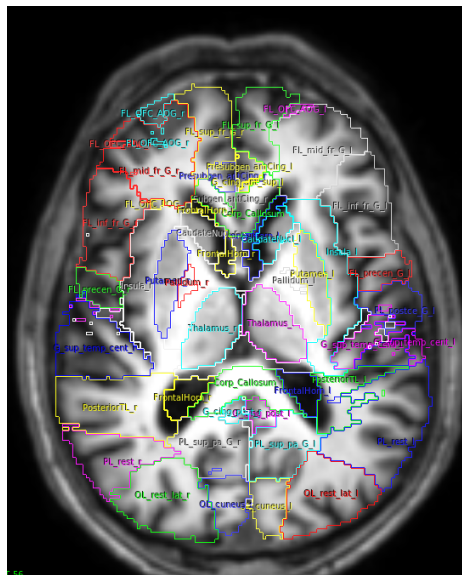


**Figure 3**

## Regions Defined by the *Hammersmith Probability Atlas*



Note. Hammersmith atlas (Hammers et al., 2003) warped into native PET space and overlaid on a co-registered MR-to-PET image.

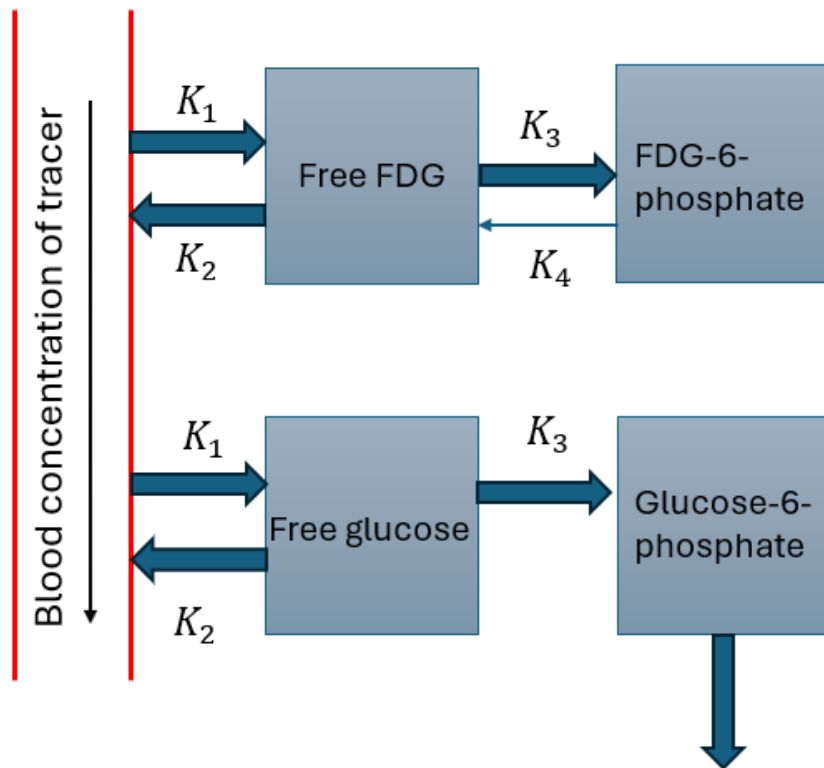
## 2.4.2 Compartmental Modelling

To estimate subject-specific delay parameters (Hinz & Turkheimer, 2006), regional time-activity curves (TACs) were fitted using compartmental models. Both three-parameter (3k) + blood volume (BV) and 4k+BV were tested. The 3k+BV model was selected for deriving the final delay values, as it provides stable estimates and avoids overfitting. Delay correction accounted for the temporal offset between the arrival of

the radiotracer in the brain and scanner timing, preventing bias when using image-derived venous input functions. These models were used for delay estimation, and the resulting values were applied to shift input functions, ensuring subsequent spectral analysis and parametric mapping reflected true tracer kinetics.

**Figure 4**

*Compartmental Model of FDG and Glucose Kinetics*



*Note.* Schematic representation of the two-tissue compartment model of FDG (top) and glucose (bottom). ‘Free FDG/ glucose’ refers to the intracellular, unmetabolised tracer/ substrate. Rate constants are:  $K_1$  (influx from blood to tissue),  $K_2$  (efflux from tissue to blood),  $K_3$  (phosphorylation), and  $K_4$  (dephosphorylation). The full model, including all four rate constants, corresponds to the  $4k + BV$  model, while the  $3K + BV$  model assumes negligible dephosphorylation of FDG.  $BV$  denotes the fractional blood volume parameter, which accounts for intravascular tracer signal. Schematic adapted from Huang et al. (1980).

#### 2.4.3 Spectral Analysis

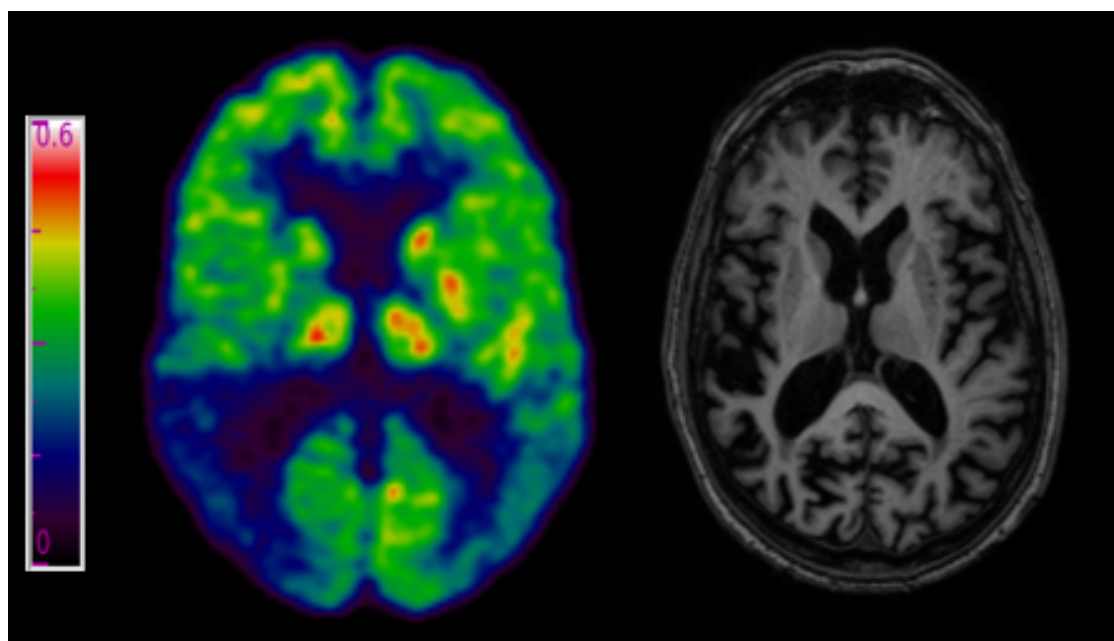
Dynamic FDG-PET data were analysed using spectral analysis (Cunningham & Jones, 1993). This estimated tracer behaviour, without assuming a fixed number of compartments, by modelling each voxels TAC as a weighted sum of exponential functions. Subject-specific delays were derived from the 3k+BV model and applied to the input function. Delay correction was set to midpoint, and zero-order hold interpolation was applied. Spectral analysis produced parametric maps for each subject, including the transport rate constant, volume of distribution, fractional BV, and model order. Visual inspection of maps was performed to check for spatial artefacts, signal drop-out, or overfitting.

#### 2.4.4 Quantification of Cerebral Glucose Metabolism

Quantitative CMRglc images were generated from the spectral analysis output. Blood glucose values were measured at baseline, 20-, 40-, and 60-minutes post-injection, and the mean value was calculated ( $\mu\text{mol}/\text{ml}/\text{min}$ ). Mean blood glucose values and a lumped constant of 0.48 were used to scale the parametric image into absolute metabolic units. The produced absolute measures of glucose metabolism.

**Figure 5**

*Parametric CMRglc Map ( $\mu\text{mol}/\text{ml}/\text{min}$ ; right) and T1-MRI (left) from a CBS-AD patient*



*Note.* Images from participant h01043.

Each CMRglc image was normalised to MNI template space in SPM12 to enable voxel-wise group-level comparison. The origin of each parametric was aligned to the structural MRI origin. Forward deformation fields were then applied to the CMRglc image using trilinear interpolation to preserve continuous voxel intensities. Regional CMRglc (rCMRglc) values were extracted from GM and unsegmented maps using the Hammersmith probabilistic atlas (Hammers et al., 2003).

As asymmetry was not lateralised to the same hemisphere across patients, scans of five patients (IDs: h00828, h01006, h01042, h01043, h01115) were flipped across the x-axis in native space and resliced using fourth-degree B-spline interpolation. This novel step standardised laterality to the left hemisphere across patients, enabling consistent group-level comparison of asymmetric pathology. The most affected hemisphere was defined clinically as contralateral to the apraxia limb.

## 2.5 Statistical analysis

### 2.5.1 VOI Analysis

Thirteen VOIs were defined based on the findings of the literature review (Table 3, Figure 7). rCMRglc values for these volumes were taken from the left hemisphere in patients. In controls, the weighted average of both hemispheres was calculated per region.

The parietal lobe VOI was derived from the Hammersmith Probabilistic Atlas and comprised the parietal lobe (1), superior parietal lobe (2), and postcentral gyrus (3). The weighted average CMRglc for the parietal lobe VOI was calculated as the sum of each constituent region's mean rCMRglc multiplied by its voxel count, divided by the total voxel count across all three regions (Figure 6). For patients, a weighted average of these constituent regions was calculated for the most affected hemisphere; for controls, the weighted average of the parietal lobe was calculated across both hemispheres.

### Figure 6

#### *Weighted Average Calculation of the Parietal Lobe*

$$\frac{(rCMRglc1 \times voxels\ 1) + (rCMRglc2 + voxels\ 2) + (rCMRglc3 + voxels\ 3)}{voxels1 + voxels2 + voxels3}$$

Data were extracted from GM TPM, except for the thalamus and pallidum. GM atrophy in these regions led to incomplete coverage and potential ventricular inclusion, so unsegmented maps were used to maximise anatomical validity.

**Table 3**

*VOIs Defined via the Hammersmith Probabilistic Atlas*

Volume	Tissue Class	Made up of
Hippocampus	GM	
Insula	GM	
Anterior Cingulate Cortex	GM	
Posterior Cingulate Cortex	GM	
Precentral Gyrus	GM	
Superior frontal gyrus	GM	
Middle frontal gyrus	GM	
Posterior Temporal Gyrus	GM	Superior temporal gyrus Middle temporal gyrus Inferior temporal gyrus
Parietal Lobe	GM	Parietal lobe Superior parietal lobe Postcentral gyrus
Caudate Nucleus	GM	
Putamen	GM	
Thalamus	Unsegmented	
Pallidum	Unsegmented	

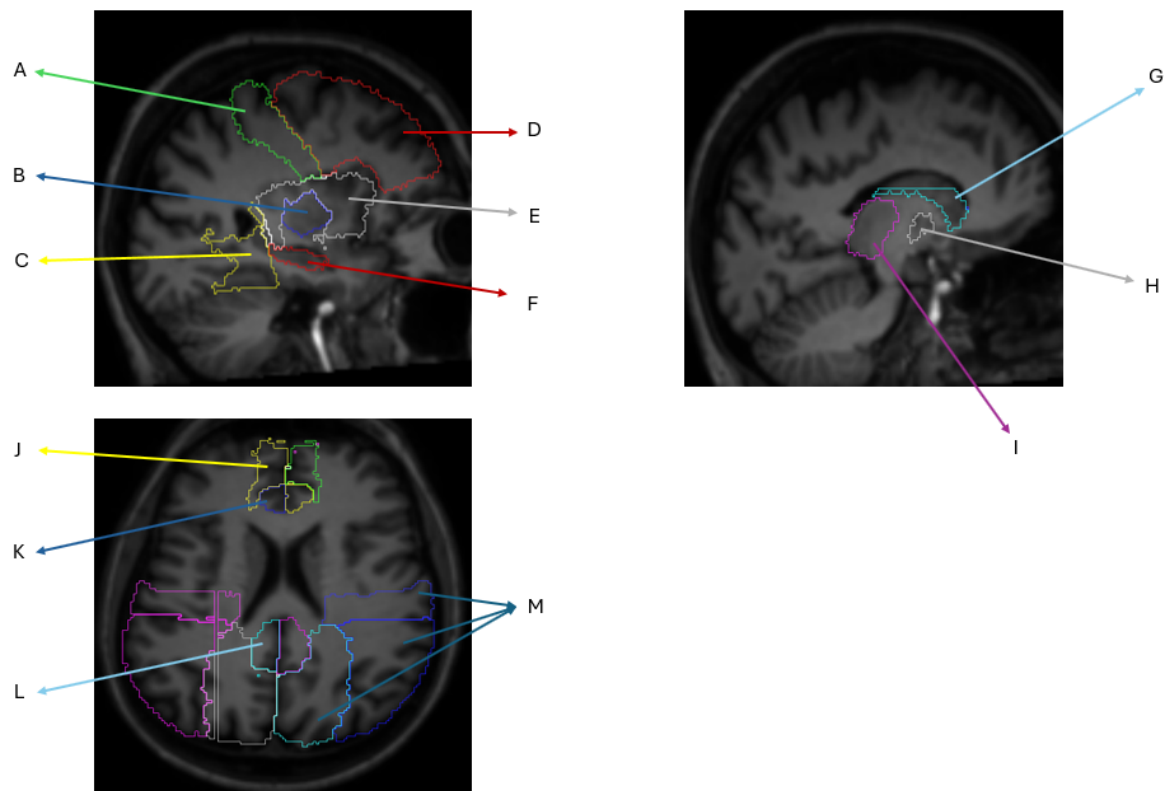
*Note.* GM: Grey matter

Normality of the rCMRglc values was assessed via the Shapiro-Wilk test, as the data violated this assumption, non-parametric testing was used. Two sets of Mann-Whitney *U* tests (two-tailed) were used to compare VOI values between groups (Controls versus Patients; CBD versus AD) in GraphPad Prism 9.5.1 (GraphPad Software, 2023). Multiple comparison was controlled using the two-stage step-up False Discovery Rate (FDR) method from Benjamini, Krieger, and Yekutieli (2006). To quantify group differences, the percentage difference between groups was calculated for each VOI. For controls versus

patients, the control group were used as the reference values. For CBS-AD versus CBS-CBD, the average median of both groups was used as the reference value.

**Figure 7**

*Atlas-defined VOIs Displayed on Co-registered MR-to-PET Images*



*Note.* A) precentral gyrus, B) putamen, C) posterior temporal lobe, D) MFG, E) insula, F) hippocampus, G) caudate nucleus, H) pallidum, I) thalamus J) superior frontal lobe K) anterior cingulate cortex L) posterior cingulate cortex M) parietal lobe.

#### 2.5.2 Voxel-wise Analysis

Voxel-wise statistical comparisons were conducted in SPM12 using the general linear model (GLM) framework. Pre-processed CMRglc images were smoothed using an 8mm FWHM Gaussian kernel and entered into two two-sample *t*-tests (Controls versus Patients; CBS-CBD versus CBS-AD). Although data deviated from normality, parametric testing in SPM12 is robust to moderate deviations; inference is based on GLM residuals and test statistics, with family-wise error (FWE) correction based on Gaussian random field theory assumptions of spatial smoothness (Friston et al., 1994; Nichols & Hayasaka, 2003). As such, permutation testing was not necessary.

The first model compared healthy controls and patients, and the second compared the two patient subgroups (CBS-CBD versus CBS-AD). In each design matrix, group membership was modelled as a separate regressor. No additional covariates (i.e., apraxia subtype, clinical scores) were included as the strong collinearity of these variables with group status risked inflating variance estimates and reducing statistical power. The dependent variable was voxel-wise CMRglc values derived from GM segmentation maps of FDG-PET data. Three contrasts were specified: controls > patients [1 -1] to identify regions of hypometabolism in patients, CBS-AD > CBS-CBD [1 -1] to identify hypometabolism in CBS-CBD, and CBS-CBD > CBS-AD [-1 1] to identify hypometabolism in CBS-AD.

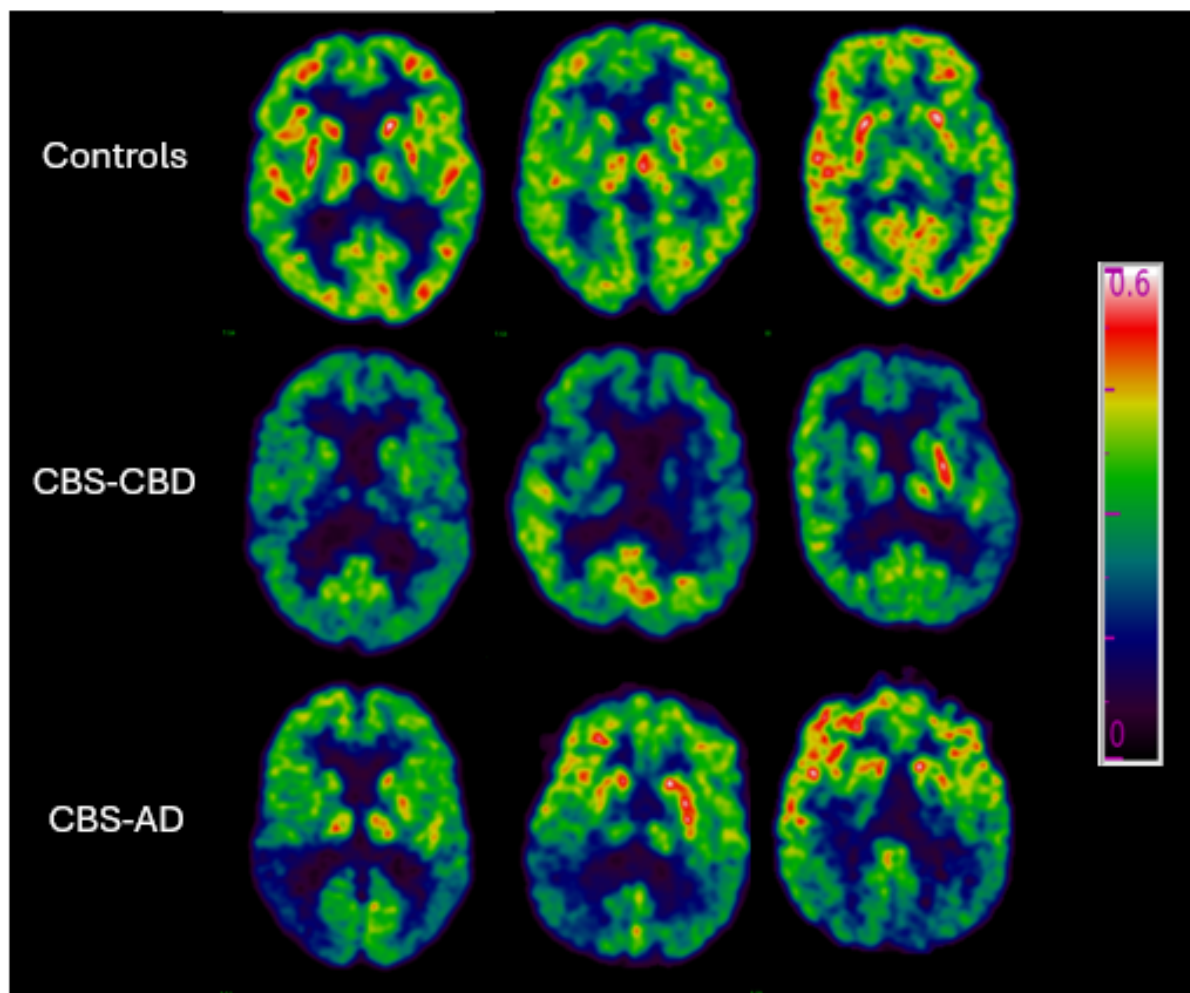
Statistical inference was performed at the voxel level to achieve precise anatomical localisation. FWE correction ( $p < .05$ ) and no cluster-extent threshold ( $k = 0$ ) were applied.

### 3. Results

Visual inspection of parametric CMRglc maps (Figure 8) revealed symmetrical glucose metabolism across GM of healthy controls. In contrast, the patient groups showed widespread asymmetrical hypometabolism and enlarged ventricles. For CBS-CBD patients, hypometabolism was localised to frontal regions. CBD-AD patients showed relative sparing of frontal regions, with hypometabolism localised to posterior regions.

**Figure 8**

*Parametric CMRglc Maps from Controls, CBS-CBD, and CBS-AD patients*



Note. Each image represents a different participant ( $n = 9$ ). Parametric maps overlaid on standard T1-weighted templates in native PET space. Colour bar represents rCMRglc values in  $\mu\text{mol}/\text{ml}/\text{min}$ .

### 3.1 VOI Analysis

Mann-Whitney *U* tests ( $p < .05$  FDR) revealed significant hypometabolism in patients ( $n = 12$ ) relative to controls ( $n = 10$ ) across 11 of 13 VOIs. Differences in the hippocampus and pallidum were not significant. The largest effects were observed in the precentral gyrus, caudate nucleus, and parietal lobe (Table 4, Figure 9).

A second Mann-Whitney *U* ( $p < .05$  FDR) analysis compared rCMRglc between CBS-CBD ( $n = 7$ ) and CBS-AD ( $n = 5$ ) patients. CBS-AD patients showed significant hypometabolism in the posterior temporal gyrus and parietal lobe compared to CBS-CBD. No significant differences were found across other VOIs (Table 5, Figure 9). One CBS-CBD patient showed abnormally high CMRglc across 10 VOIs.

**Table 4**

*Percentage Difference in Median rCMRglc ( $\mu\text{mol}/\text{ml}/\text{min}$ ) between controls and patients (controls – patients)*

VOI	Median Controls	Median Patients	% Difference	p-value (FDR)	U statistic
Hippocampus	.206	.178	-14%	.069	32
Insula	.282	.239	-15%	.002**	15
Anterior Cingulate	.304	.263	-13%	.030*	27
Posterior cingulate	.361	.299	-17%	.003**	16
Precentral gyrus	.338	.239	-29%	<.001***	8
Superior frontal gyrus	.333	.264	-21%	.002**	15
Middle frontal gyrus	.332	.291	-12%	<.001***	10
Posterior temporal gyrus	.287	.203	-29%	.003**	17
Parietal lobe	.315	.229	-27%	.003**	16
Caudate nucleus	.345	.231	-33%	<.001***	0
Putamen	.313	.338	8%	.025*	26
Thalamus	.265	.187	-29%	.001**	13
Pallidum	.234	.229	-2%	.283	43

Note. Negative values indicate rCMRglc patients < rCMRglc controls; positive values indicate rCMRglc patients > rCMRglc controls.

Asterisks denote significance level (\* =  $p < .05$ , \*\* =  $p < .01$ , \*\*\* =  $p < .001$ ).

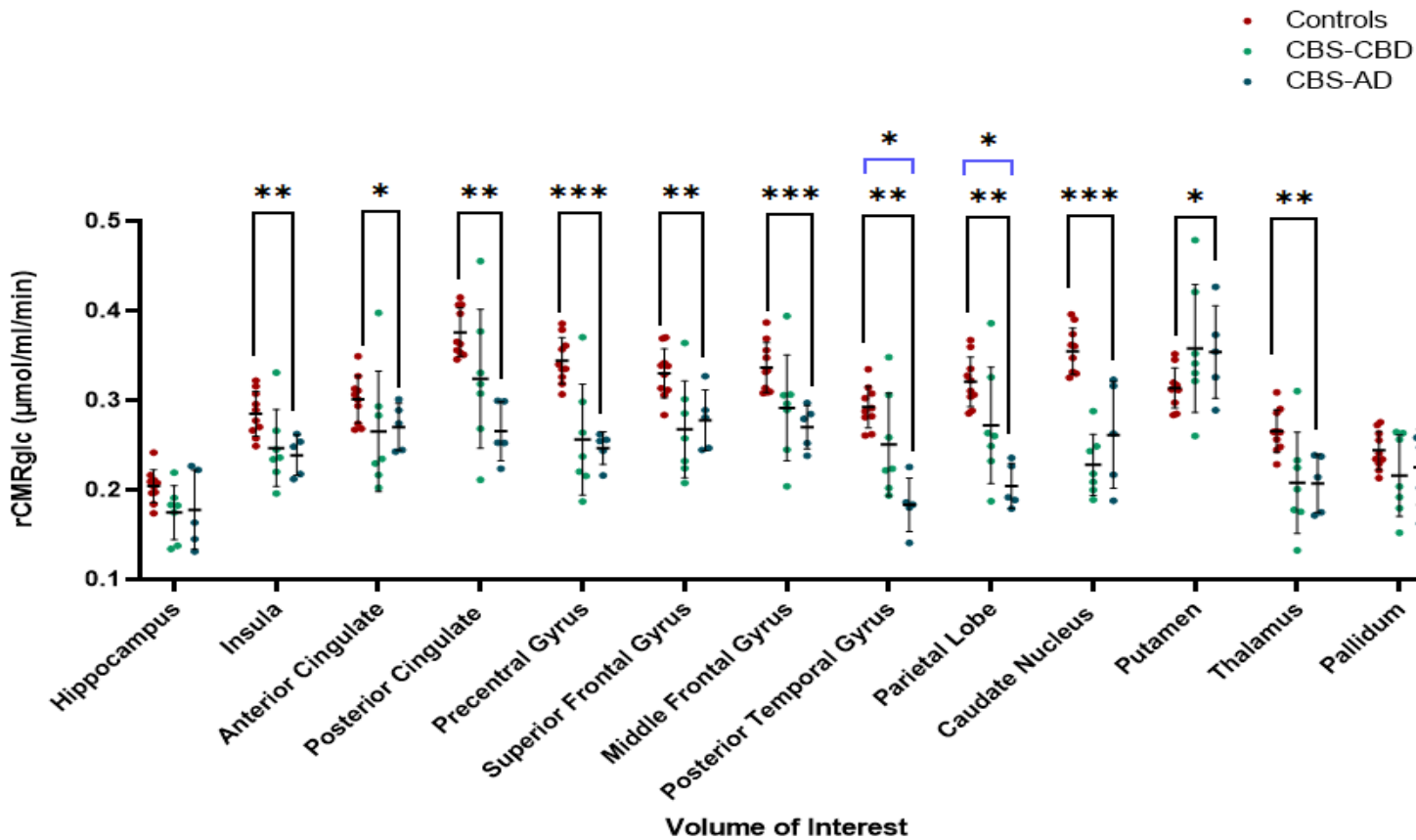
**Table 5***Percentage Difference in Median rCMRglc  $\mu\text{mol}/\text{ml}/\text{min}$  (CBS-AD – CBS-CBD)*

VOI	Median CBS-AD	Median CBS-CBD	% Difference	p-value (FDR)	U statistic
Hippocampus	.163	.182	-11%	>.999	17
Insula	.248	.236	5%	>.999	17
Anterior Cingulate	.274	.234	16%	.432	12
Posterior cingulate	.253	.318	-23%	.106	7
Precentral gyrus	.254	.237	7%	>.999	17
Superior frontal gyrus	.281	.257	9%	.639	14
Middle frontal gyrus	.279	.296	-6%	.343	11
Posterior temporal gyrus	.184	.223	-19%	.030*	4
Parietal lobe	.192	.249	-26%	.048*	5
Caudate nucleus	.217	.218	-0.5%	.431	12
Putamen	.354	.341	-4%	.876	16
Thalamus	.214	.201	6%	>.999	17
Pallidum	.228	.204	11%	>.999	17

Note. Positive values indicate rCMRglc CBS-AD > CBS-CBD; negative values indicate rCMRglc CBS-AD < CBS-CBD a lower median in CBS-CBD. \* =  $p < .05$ .

**Figure 9**

*rCMR<sub>glc</sub> values in Controls and CBS Subgroups: Mann-Whitney U Test Results*



Note. Asterisks denote significance level (\* =  $p < .05$ , \*\* =  $p < .01$ , \*\*\* =  $p < .001$ ). Black brackets indicate the results from the Mann-Whitney *U* test comparing controls and patients; blue brackets indicate significant results from the Mann-Whitney *U* test comparing CBS-AD and CBS-CBD patient subgroups.

### 3.2 Voxel-wise Analysis

Voxel-wise two-sample *t*-tests ( $p < .05$  FWE) revealed hypometabolism in patients relative to controls across several regions (Table 6, Figure 10). No significant differences were found for comparison between the two patient groups (CBD > AD, or AD > CBD).

**Table 6**

*Peak Voxel-wise Hypometabolism in Patients Relative to Controls*

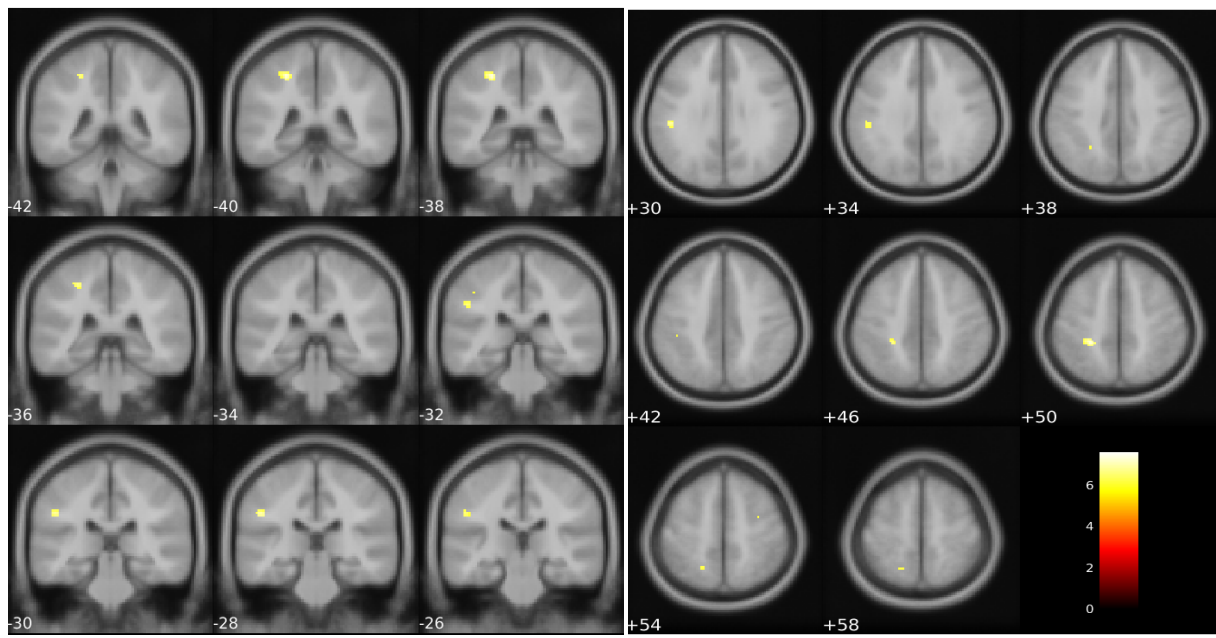
Region	Hemisphere	T-statistic	<i>p</i> -FWE	MNI		
				x	y	z
SPL	L	7.56	.005	-26	-39	50
		6.47	.028	-18	-57	56
		6.34	.035	-22	-54	64
		6.28	.039	-24	-52	39
Supramarginal Gyrus	L	6.99	.012	-48	-28	32
		6.17	.047	-42	-33	44
Precentral Gyrus	R	6.34	.036	32	-4	52
		6.62	.041	58	9	32
Middle Frontal Gyrus	L	6.26	.040	-27	18	44

Note. SPL: Superior parietal lobule. Peak coordinates are reported in MNI space.

Inference was conducted at the voxel level with FWE correction at  $p < .05$  ( $k = 0$ ).

**Figure 10**

*Montage of Voxel-wise Hypometabolism in Patients Relative to Controls*



Note. Coronal montage (left) showing every 2<sup>nd</sup> slice collected from slice -42 to -26.

Axial montage (right) showing every 4<sup>th</sup> slice collected from slice 30 to 58. The colour bar indicates voxel-wise T-statistics, thresholded at  $p < .05$  (voxel level).

## 4. Discussion

The aim of this study was to compare cerebral glucose metabolism patterns in CBS and its underlying pathologies. Given that CBS is a highly heterogeneous syndrome with limited diagnostic specificity (Alexander et al., 2014), identifying imaging patterns may serve as disease-specific markers.

### 4.1 Patients versus Controls

In comparison to healthy controls, patients with CBS exhibited widespread hypometabolism encompassing both cortical and subcortical regions. This finding aligns with the study hypotheses and is consistent with prior studies reporting significant metabolic impairment in CBS (Pardini et al., 2019). Additionally, it aligns with the clinically observed motor and cognitive deficits (Armstrong et al., 2013; Aiba et al., 2023; Shir et al., 2023). These findings support the pronounced involvement of frontoparietal networks, highlighting their significance as a principal substrate for CBS phenotypes.

The most pronounced regions of hypometabolism in patients were localised to the precentral gyrus, MFG, and caudate nucleus. Dysfunction within the precentral gyrus was expected, given that motor deficits are a core feature of CBS and this region is involved in initiating voluntary movements in contralateral limbs (Armstrong, 2013; Banker & Tadi, 2019). Previous research identified a negative correlation between atrophy in the precentral cortex and ideomotor apraxia (Huey et al., 2010), suggesting this hypometabolism likely underlies apraxia symptoms in CBS. Unexpectedly, voxel-wise analysis revealed precentral hypometabolism in the ipsilateral hemisphere. Although this hints at bilateral involvement, it is an isolated finding and other patterns of hypometabolism highlight the characteristic asymmetry of CBS. Overall, precentral cortex hypometabolism provides a neuroanatomical basis for motor impairments, particularly the execution of learned, purposeful movements, in CBS.

The MFG, implicated in executive function tasks such as working memory, attention, and planning (Royall et al., 2002), also showed significant hypometabolism in patients. Metabolic dysfunction in this region reinforces the view of CBS as a cognitive disorder, and not purely a motor output disorder. Reduced metabolism may reflect disruption of

executive processes involved in translating action representations into motor outputs, manifesting as impaired gesture sequencing and copying to command.

Caudate hypometabolism was expected due to subcortical involvement in CBS. This network-level dysfunction across cortical and subcortical regions may explain why motor and cognitive symptoms co-occur. Evidence from PET and stimulation studies has highlighted the caudate's role in motor initiation, timing, and action selection (Carbon et al., 2004; Wilburn & Kesner, 1974). Carbon et al. (2004) reported that coupling of dopaminergic input to the caudate with thalamocortical networks is disrupted in Parkinson's disease, leading to impaired motor learning. Thus, caudate hypometabolism likely underscores Parkinsonian motor rigidity observed in CBS patients.

Unexpectedly, the putamen showed significant hypermetabolism in patients relative to controls, contrasting with the hypothesised hypometabolism. Relative hypermetabolism in the putamen has been a consistent yet debated finding in Parkinson's disease. Eidelberg et al. (1994) reported putaminal hypermetabolism in Parkinson's patients, proposing that this overactivity is the result of reduced dopaminergic input from the substantia nigra, which reduces inhibitory control of the basal ganglia. Others, namely Borghammer et al. (2009a, 2009b) suggest hypermetabolism represents a methodological artefact, in which scaling the image to the global mean artificially inflates signal across subcortical regions, reflecting biased normalisation procedures. However, in the present study, hypometabolism was observed in other subcortical regions such as the thalamus. Importantly, the study used absolute rCMRglc values, avoiding proportional scaling to the global mean. This suggests the present hypermetabolism observed in the putamen was driven by true biological processes, rather than a methodological artefact.

These patterns of glucose metabolism underscore how CBS is a network-level disorder, involving both cortical and subcortical systems. CBS disrupts the frontostriatal circuits involved in integrating higher-order motor planning with movement initiation and execution. This helps explain the combination of impaired motor programs, cognitive deficits, and extrapyramidal features.

## 4.2 CBS-AD versus CBS-CBD

While both subgroups showed frontoparietal hypometabolism, VOI analysis identified pronounced temporoparietal hypometabolism in CBS-AD patients. Given the spatial distribution of A $\beta$  plaques and neurofibrillary tau tangles is focused in posterior temporoparietal regions in CBS-AD, this subgroup difference was expected (Constantinides et al., 2019). These findings also align with prior evidence suggesting that CBS-AD shares similarities with typical AD in its posterior cortical involvement and relative sparing of deep GM (Constantinides et al., 2019; Pardini et al., 2019). CBS-CBD patients did not show any distinct regions of hypometabolism relative to AD, with impaired metabolism confined to the common frontoparietal regions.

These diverging hypometabolic patterns correspond to distinct apraxia profiles. CBS-AD patients typically present with failures in gesture imitation, reflecting posterior contributions to representational aspects of praxis. Conversely, CBS-CBD patients, with predominant motor and frontoparietal dysfunction, tend to fail on copying to command and imitation, reflecting impaired translation of action representations into motor executions. Thus, while both groups converge clinically on apraxia, the neural basis of their deficits differs. This provides a mechanistic explanation for how distinct pathological substrates result in similar symptoms.

Surprisingly, no significant hypometabolism was observed in the hippocampus. Hypometabolism in this region was hypothesised in the CBS-AD group given the established role of hippocampal dysfunction in AD (Constantinides, 2019). A similar observation was reported by Josephs et al. (2010), who noted relative sparing of hippocampi in CBS-AD and CBS-CBD. One potential explanation is that CBS-AD represents an atypical form of Alzheimer's disease. In this form, pathology may preferentially target posterior cortical regions, rather than medial temporal structures. This posterior variant of AD has been described in other studies, where parietal hypometabolism dominates AD pathology (Pardini et al., 2019). Alternatively, there may be a methodological explanation: hippocampi are small, making them prone to PVEs, particularly if atrophied. Without PVC, true hypometabolism may be underestimated, which may have contributed to the lack of significant findings.

Participant h00559, diagnosed with CBS-CBD, showed unusually high FDG uptake across 10 VOIs, even relative to control participants. Given that this elevation is observed consistently, it likely reflects a systematic shift in measurements as FDG-PET is highly sensitive to the scanning environment. Patient and control scans were obtained under different conditions by different researchers, so subtle methodological differences may account for this. Alternatively, it may be due to an altered internal state of the patient. This possibility warrants further investigation and potential exclusion of this participant from the analysis.

#### 4.3 VOI and Voxel-Wise Analysis

VOI analysis identified more group differences than voxel-wise analysis. Hypometabolism was observed in most predefined regions for patients compared to controls, as well as subtle distinctions between CBS-AD and CBS-CBD in temporoparietal regions, which voxel-wise analysis did not detect. This was anticipated due to the increased statistical power of VOI from averaging the signal across smaller regions (Greve et al., 2014).

VOI analysis also identified additional subcortical differences (in the putamen and thalamus) not revealed by voxel-wise analysis. This discrepancy may stem from VOI's increased statistical power or its susceptibility to spillover effects. These regions are small and likely atrophic in patients, so increased CSF within the VOI (e.g., from the ventricles) may have distorted rCMRglc values. Atlas-based VOI methods are limited in neurodegenerative diseases as regional atrophy and ventricular enlargement disrupt the alignment between patient anatomy and standard atlases. This can enhance the risk of misclassification of tissue and spillover effects. However, prior to receiving the data, frame-to-frame realignment corrected for head motion and resolution-modelling image reconstruction improved the spatial resolution of images, thereby mitigating the need for PVC (Dinelle et al., 2011; Walker et al., 2011). It is therefore more likely that the increased statistical power of VOI contributes to these additional results, rather than methodological issues of VOI analysis.

Voxel-wise analysis yielded a more restricted set of results for patients compared to controls. Hypometabolism was observed in the superior parietal lobule, precentral

gyrus, supramarginal gyrus, and MFG, with no significant differences between patient subgroups. Voxel-wise analysis allowed more precise localisation, highlighting focal hypometabolism in the supramarginal gyrus. This suggests this region is a focal point of dysfunction, consistent with the broader parietal effects observed in VOI analysis. As VOI analysis is restricted by atlas boundaries, focal effects may be averaged across broader regions, masking regional heterogeneity. Consequently, its capacity for precise localisation is reduced compared to voxel-wise analysis.

Further, the restricted results in voxel-wise analysis may reflect differences in multiple comparison correction. Voxel-wise analyses were corrected using FWE, a more conservative approach than the FDR correction applied to VOI analysis. This reduces the risk of false positives but may also limit sensitivity to true effects. In addition, voxel-wise analysis is less susceptible to PVEs, as it only analyses regions classified as GM. This further reduces the false signal in atrophied regions. While a core strength of the present study is its use of absolute rCMRglc values, this violates conventional assumptions of voxel-wise analysis, which is optimised for relative, rather than absolute, values. Had the data been normalised to a global mean, additional significant effects may have appeared, particularly in subgroup analysis.

Caution is needed when interpreting results from both types of analysis; however, employing both analytical techniques strengthens the validity of the present findings. Both approaches converge on key findings, revealing widespread frontoparietal dysfunction in CBS patients. This demonstrates the value of assessing metabolism over volumes (VOI) while mapping localised effects using voxel-wise analysis.

#### 4.4 Strengths and limitations

The complementary application of VOI and voxel-wise analysis is a key strength of the present study. Outcomes are not skewed by the analysis approach, thereby improving validity. By combining hypothesis-driven VOIs with voxel-wise exploratory mapping, the study achieved a balance between sensitivity and openness to unexpected results. This enhanced interpretability while minimising bias in the findings.

The study benefited from stratifying CBS patients based on their underlying pathology, rather than treating them as a uniform group, addressing the clinicopathological

heterogeneity of the syndrome. With this approach, the study identified syndrome variability and revealed pathology-specific patterns of metabolism, directly addressing the study aim. The pathological distinction offers mechanistic insight into how different pathologies converge on the shared clinical presentation of CBS yet exhibit distinct FDG-PET patterns. Moreover, this pathology-based stratification aligns with current frameworks, which are increasingly relying on biomarkers to distinguish underlying diseases. By aligning with this trend, findings are applicable to translational research and clinical trials.

Additionally, the study utilised a HRRT PET scanner, which provides superior spatial resolution compared to standard PET scans. Combined with resolution-modelling image reconstruction, this increases confidence in the regional specificity of the results. Confidence is further enhanced through the incorporation of T1 MRI scans for co-registration and segmentation, which enables anatomical localisation of the PET signal.

The anatomical MRI scans were, however, only used for processing purposes and not for analysis. This prevented an assessment of how atrophy contributed to the observed hypometabolism. Without quantification of GM loss, it is difficult to disentangle hypometabolism due to neural dysfunction from the secondary effects of atrophy. A multimodal approach combining FDG-PET with cortical thickness measures would have enabled more rigorous dissection of functional versus structural contributions to hypometabolism.

The absence of pathological confirmation within the study cohort reduces diagnostic validity. Without autopsy-confirmed diagnoses, group stratification relies on clinical criteria, which carry limited specificity (Shir et al., 2023). Therefore, it is possible that some patients were misdiagnosed, blurring the distinction between CBS-AD and CBS-CBD. This would undermine the central aim of differentiating underlying pathology; therefore, analysis of *in vivo* CSF biomarkers would have provided useful confirmation. Although this is an important caveat, the close alignment of the present findings with those of Pardini et al. (2019), who studied a pathologically confirmed cohort, mitigates these concerns, suggesting the clinical diagnosis within the sample was correct.

Replication across multiple pathologically confirmed cohorts is required to confirm this, however.

The study is further limited by the sample size. Due to the rarity of CBS, the sample was small, with only 5 CBS-AD and 7 CBS-CBD patients. This reduces the statistical power of the study, especially in voxel-wise analysis, where power is already limited. This may explain the lack of patient group differences identified with this analysis approach. Moreover, this amplifies the influence of outliers, where anomalously high FDG uptake could bias group-level results.

Finally, the study is also limited by its cross-sectional design, which only captures a single time point in disease progression. As a result, findings cannot reveal whether hypometabolism reflects early dysfunction or irreversible late-stage decline. This is compounded by the fact that patients were recruited at varying stages of their disease, introducing clinical and imaging heterogeneity. This prevented any meaningful correlations between imaging profiles and clinical data (i.e., UPDRS or MMSE), which would have linked metabolic abnormalities to symptom severity and progression. CBS-CBD patients initially present with gait disturbances and falls, followed by later cognitive impairment and behavioural changes, whereas AD cases are typically characterised by early cognitive impairments and personality changes throughout the disease course (Aiba et al., 2023). Without longitudinal data, these dynamic symptom-metabolisms relationship remain unresolved, limiting our ability to determine the temporal sequence of network dysfunction. Although distinct metabolic patterns were identified, their clinical interpretability remains limited, and further work is needed to disentangle how underlying pathology drives the evolution of metabolism and phenotype over the disease course.

#### 4.5 Future Directions

In light of these limitations, future research should employ a longitudinal design with a larger, pathologically confirmed cohort. This would enable correlation between metabolic patterns and symptom progression over time, providing insight into their temporal relationship. For example, research could investigate whether frontoparietal cortical hypometabolism precedes the onset of motor symptoms, such as alien limb

syndrome, or if posterior hypometabolism is associated with visuospatial deficits. However, it is important to note that while the UPDRS is validated for Parkinson's, it is not specifically designed for CBS, and there are no universally accepted apraxia batteries. This lack of standardisation reduces the reliability of clinical assessments. Developing a standardised assessment would provide a stronger clinical basis for interpreting the relationship between imaging and clinical data. Addressing these questions would provide insight into disease progression and inform optimal timing of therapeutic interventions. Crucially, these studies should also aim to distinguish the metabolic profiles of other CBS pathologies (i.e., LBD, FTLD, and PSP). This will provide a more complete set of metabolic patterns across the spectrum of CBS, enabling reliable differentiation of non-AD pathologies, which is currently limited. Incorporating MRI data would also reduce the confounding effects of atrophy. This would help disentangle true metabolic deficits from volume loss artefacts.

Larger, longitudinal datasets would also facilitate the training of machine-learning (ML) algorithms for diagnosis. Due to the small sample size in the present study, it was not possible to assess whether FDG-PET can distinguish between pathologies at the individual level. With larger data sets, it would be possible to produce a receiver operating curve looking at the parietal-frontal ratios, providing a quantitative threshold for individual diagnosis. This could then be applied to ML studies to improve diagnosis of underlying pathologies in CBS. Recent research from Barnard et al. (2025) demonstrates the feasibility of ML for diagnosis. Their tool, StateViewer, achieved high diagnostic accuracy ( $AUC = 0.93 \pm 0.02$ , sensitivity =  $0.89 \pm 0.03$ ) across nine neurodegenerative diseases. However, CBS was treated as a single group in that study, underscoring the need for future models to differentiate between pathologies. Implementing such algorithms in clinical practice could provide data-driven support to enhance stratification in therapeutic trials and improve diagnostic confidence for patients presenting with CBS.

To further characterise the network abnormalities revealed in the present study, future multimodal imaging studies should incorporate diffusion-weighted imaging (DWI). By quantifying the microstructural integrity of WM tracts through metrics such as fractional anisotropy and mean diffusivity, DWI can reveal how pathological processes in CBS

disrupt large-scale networks (i.e., frontostriatal and frontoparietal pathways). Assessing whether structural disconnection in WM tracts, such as the corticospinal tract or superior longitudinal fasciculus, predicts motor and apraxia symptoms could clarify the mechanistic basis of CBS phenotypes. Moreover, Feany and Dickson (1995) highlight how, while WM tracts remain intact in CBS-AD, they show significant myelin pallor and gliosis in CBS-CBD. Testing WM degradation could potentially offer complementary insight into distinguishing underlying pathology.

#### 4.6 Clinical and Theoretical Implications

The finding that CBS pathology can be distinguished through glucose metabolism patterns has important diagnostic implications. Currently, the most widely used biomarker for CBS-AD is low A $\beta$ 42, accompanied by elevated tau in CSF. This demonstrates good sensitivity for CBS-AD; however, CSF biomarkers have limited specificity for non-AD pathologies (Constantinides et al., 2019). Amyloid deposition is also common in cognitively normal older adults, reducing diagnostic reliability (Jansen et al., 2015). As a result, many patients receive the unclear diagnosis of ‘CBS-nonAD’, which hinders prognosis and access to relevant trials. FDG-PET reveals topographically distinct patterns of hypometabolism that correspond to various pathologies. These metabolic signatures can complement CSF markers and refine *in vivo* diagnosis, especially for non-AD pathologies. By stratifying patients beyond binary AD versus non-AD categories, treatment and access to relevant therapeutic trials improve.

Accurate diagnosis helps patients access disease-specific care. If FDG-PET and CSF biomarkers indicate CBS-AD pathology, patients can receive Alzheimer’s medications such as acetylcholinesterase inhibitors (NICE, 2018) or emerging amyloid-targeting therapies, such as aducanumab and lecanemab, which have shown promising early clinical benefits by reducing amyloid plaques (Delpirou Nouh & Younes, 2024). Confirming AD pathology also justifies early counselling and planning for Alzheimer’s-like disease course (i.e., progressive memory and visuospatial decline). In contrast, if biomarkers suggest CBS-CBD, clinicians can avoid AD-specific drugs, which are unlikely to help. This reduces unnecessary drug exposure and prioritises symptomatic and supportive treatments, such as Parkinsonian therapies. Accurate diagnosis

prevents a ‘one size fits all’ approach and enables more appropriate, effective treatment choices.

Improved diagnostic stratification using imaging and CSF biomarkers is key to successful trials. Research often uses molecular biomarkers in trial enrolment to identify AD pathology - FDG-PET can aid further CBS stratification, creating more homogeneous cohorts with predictable symptom paths. Trials can then pre-specify endpoints according to the underlying pathology. For example, cognition-dominant endpoints are suitable for CBS-AD, while motor endpoints are more suitable for CBS-CBD. Accurate patient subgroups also increase sensitivity to detecting true treatment effects.

However, there are some caveats regarding FDG-PET as a diagnostic biomarker. Access to PET remains limited outside specialised centres, with high costs and limited tracer availability, making its clinical utility restricted compared to CSF. As mentioned earlier, interpretation of results can be confounded by PVE from atrophy, which may obscure subtle disease-specific differences unless corrected. These limitations underscore the need for multimodal frameworks that integrate FDG-PET with structural MRI to enhance diagnostic specificity. While replication in larger, autopsy-confirmed cohorts is required, the present findings demonstrate the translational potential of FDG-PET as a diagnostic marker of underlying CBS pathology.

The present findings also contribute to theoretical models of CBS by demonstrating how distinct pathologies converge on the same clinical syndrome through different dysfunctional networks. The primary motor cortex showed significant hypometabolism in CBS compared to healthy controls. However, this did not differ between patient subgroups. This suggests that dysfunction of the motor cortex may be a necessary common pathway for the CBS phenotype, leading to asymmetric rigidity and apraxia, irrespective of the underlying proteinopathy. Despite this convergence, FDG-PET patterns reveal distinct differences between the metabolic profiles of underlying pathologies. The clinical presentation of CBS-AD is dominated by cognitive features, with the underlying network disruptions revealing hypometabolism of temporoparietal regions, which is not evident in CBS-CBD. These diverging patterns of hypometabolism support the view that CBS is not a unitary disorder, but a syndrome at the intersection of

multiple diseases. Findings also support the network dysfunction hypothesis (Palop et al., 2006). This theory suggests that neurodegeneration spreads through the disruption of synaptic activity within large-scale neural networks, mediated by the abnormal accumulation of proteins. By disentangling the overlapping and distinct metabolic profiles of CBS-AD and CBS-CBD, these findings enrich theoretical accounts of how neurodegenerative diseases propagate through the brain, and how specific networks shape clinical manifestations.

#### 4.7 Conclusion

In summary, CBS I characterised by widespread frontoparietal and subcortical dysfunction, with distinct metabolic patterns for CBS-CBD and CBS-AD. Both pathologies involve motor cortex dysfunction, but CBS-AD shows additional temporoparietal hypometabolism. FDG-PET, therefore, offer potential pathology-specific markers which extend beyond AD versus non-AD classification. The complementary use of VOI and voxel-wise analysis validates the results of converging findings; VOI enhanced power to detect group differences, while voxel-wise provided finer localisation. Overall, findings provide a framework for combining multimodal imaging to enhance diagnosis, inform trial design, and enrich theoretical accounts of CBS resulting from network dysfunction.

## 5. References

- Aiba, I., Hayashi, Y., Shimohata, T., Yoshida, M., Saito, Y., Wakabayashi, K., Komori, T., Hasegawa, M., Ikeuchi, T., Tokumaru, A. M., Sakurai, K., Murayama, S., Hasegawa, K., Uchihara, T., Toyoshima, Y., Saito, Y., Yabe, I., Tanikawa, S., Sugaya, K., ... Nakashima, K. (2023). Clinical course of pathologically confirmed corticobasal degeneration and corticobasal syndrome. *Brain Communications*, 5(6), fcad296. <https://doi.org/10.1093/braincomms/fcad296>
- Albrecht, F., Bisenius, S., Morales Schaack, R., Neumann, J., & Schroeter, M. L. (2017). Disentangling the neural correlates of corticobasal syndrome and corticobasal degeneration with systematic and quantitative ALE meta-analyses. *NPJ Parkinson's Disease*, 3(1), Article 12. <https://doi.org/10.1038/s41531-017-0012-6>
- Alexander, S. K., Rittman, T., Xuereb, J. H., Bak, T. H., Hodges, J. R., & Rowe, J. B. (2014). Validation of the new consensus criteria for the diagnosis of corticobasal degeneration. *Journal of Neurology, Neurosurgery and Psychiatry*, 85(8), 925–929. <https://doi.org/10.1136/jnnp-2013-307035>
- Armstrong, M. J., Litvan, I., Lang, A. E., Bak, T. H., Bhatia, K. P., Borroni, B., Boxer, A. L., Dickson, D. W., Grossman, M., Hallett, M., Josephs, K. A., Kertesz, A., Lee, S. E., Miller, B. L., Reich, S. G., Riley, D. E., Tolosa, E., Tröster, A. I., Vidailhet, M., & Weiner, W. J. (2013). Criteria for the diagnosis of corticobasal degeneration. *Neurology*, 80(5), 496–503. <https://doi.org/10.1212/WNL.0b013e31827f0fd1>
- Ashburner, J., & Friston, K. J. (2000). Voxel-Based Morphometry—The Methods. *NeuroImage (Orlando, Fla.)*, 11(6), 805–821. <https://doi.org/10.1006/nimg.2000.0582>
- Ashburner, J., & Friston, K. J. (2005). Unified segmentation. *NeuroImage (Orlando, Fla.)*, 26(3), 839–851. <https://doi.org/10.1016/j.neuroimage.2005.02.018>
- Banker, L., & Tadi, P. (2019). Neuroanatomy, precentral gyrus.

Barnard, L., Botha, H., Corriveau-Lecavalier, N., Graff-Radford, J., Dicks, E., Gogineni, V., Zhang, G., Burkett, B. J., Johnson, D. R., Huls, S. J., Khurana, A., Stricker, J. L., Paul Min, H.-K., Senjem, M. L., Fan, W. Z., Wiste, H., Machulda, M. M., Murray, M. E., Dickson, D. W., ... Jones, D. T. (2025). An FDG-PET-Based Machine Learning Framework to Support Neurologic Decision-Making in Alzheimer Disease and Related Disorders. *Neurology*, 105(2), Article e213831.

<https://doi.org/10.1212/WNL.0000000000213831>

Benjamini, Y., Krieger, A. M., & Yekutieli, D. (2006). Adaptive linear step-up procedures that control the false discovery rate. *Biometrika*, 93(3), 491–507.

<https://doi.org/10.1093/biomet/93.3.491>

Boeve, B. F., Lang, A. E., & Litvan, I. (2003). Corticobasal degeneration and its relationship to progressive supranuclear palsy and frontotemporal dementia. *Annals of Neurology*, 54(S5), S15–S19.

<https://doi.org/10.1002/ana.10570>

Borghammer, P., Cumming, P., Aanerud, J., & Gjedde, A. (2009a). Artefactual subcortical hyperperfusion in PET studies normalized to global mean: Lessons from Parkinson's disease. *NeuroImage (Orlando, Fla.)*, 45(2), 249–257.

<https://doi.org/10.1016/j.neuroimage.2008.07.042>

Borghammer, P., Cumming, P., Aanerud, J., Förster, S., & Gjedde, A. (2009b). Subcortical elevation of metabolism in Parkinson's disease — A critical reappraisal in the context of global mean normalization. *NeuroImage (Orlando, Fla.)*, 47(4), 1514–1521. <https://doi.org/10.1016/j.neuroimage.2009.05.040>

Boxer, A. L., Geschwind, M. D., Belfor, N., Gorno-Tempini, M. L., Schauer, G. F., Miller, B. L., & Weiner, M. W. (2006). Patterns of brain atrophy that differentiate corticobasal degeneration syndrome from progressive supranuclear palsy. *Archives of Neurology*, 63(1), 81–86. <https://doi.org/10.1001/archneur.63.1.81>

Buxbaum, L. J. (2001). Ideomotor Apraxia: a Call to Action. *Neurocase*, 7(6), 445–458.

<https://doi.org/10.1093/neucas/7.6.445>

- Caixeta, L., Caixeta, V. de M., Nogueira, Y. L., & Aversi-Ferreira, T. A. (2020). Pharmacological interventions in corticobasal degeneration: a review. *Dementia & Neuropsychologia*, 14(3), 243–247. <https://doi.org/10.1590/1980-57642020dn14-030006>
- Carbon, M., Ma, Y., Barnes, A., Dhawan, V., Chaly, T., Ghilardi, M. F., Eidelberg, D. (2004). Caudate nucleus: Influence of dopaminergic input on sequence learning and brain activation in parkinsonism. *NeuroImage*, 21(4), 1497–1507. <https://doi.org/10.1016/j.neuroimage.2003.12.014>
- Carter, S. F., Caine, D., Burns, A., Herholz, K., & Lambon Ralph, M. A. (2012). Staging of the cognitive decline in Alzheimer's disease: insights from a detailed neuropsychological investigation of mild cognitive impairment and mild Alzheimer's disease. *International Journal of Geriatric Psychiatry*, 27(4), 423–432. <https://doi.org/10.1002/gps.2738>
- Carter, S. F., Embleton, K. V., Anton-Rodriguez, J. M., Burns, A., Ralph, M. A. L., & Herholz, K. (2014). Regional Neuronal Network Failure and Cognition in Late-Onset Sporadic Alzheimer Disease. *American Journal of Neuroradiology : AJNR*, 35(Supplement 6), S18–S30. <https://doi.org/10.3174/ajnr.A3895>
- Constantinides, V. C., Paraskevas, G. P., Efthymiopoulou, E., Stefanis, L., & Kapaki, E. (2019). Clinical, neuropsychological and imaging characteristics of Alzheimer's disease patients presenting as corticobasal syndrome. *Journal of the Neurological Sciences*, 398, 142–147. <https://doi.org/10.1016/j.jns.2019.01.046>
- Cunningham, V. J., & Jones, T. (1993). Spectral Analysis of Dynamic PET Studies. *Journal of Cerebral Blood Flow and Metabolism*, 13(1), 15–23. <https://doi.org/10.1038/jcbfm.1993.5>
- Day, G. S., Lim, T. S., Hassenstab, J., Goate, A. M., Grant, E. A., Roe, C. M., Cairns, N. J., & Morris, J. C. (2017). Differentiating cognitive impairment due to corticobasal degeneration and Alzheimer disease. *Neurology*, 88(13), 1273–1281. <https://doi.org/10.1212/WNL.0000000000003770>

- de Jong, H. W. A. M., van Velden, F. H. P., Kloet, R. W., Buijs, F. L., Boellaard, R., & Lammertsma, A. A. (2007). Performance evaluation of the ECAT HRRT: an LSO-LYSO double layer high resolution, high sensitivity scanner. *Physics in Medicine & Biology*, 52(5), 1505–1526. <https://doi.org/10.1088/0031-9155/52/5/019>
- Delpirou Nouh, C., & Younes, K. (2024). Diagnosis and Management of Progressive Corticobasal Syndrome. *Current Treatment Options in Neurology*, 26(7), 319–338. <https://doi.org/10.1007/s11940-024-00797-4>
- Dickson, D. W., Bergeron, C., Chin, S. S., Duyckaerts, C., Horoupien, D., Ikeda, K., Jellinger, K., Lantos, P. L., Lippa, C. F., Mirra, S. S., Tabaton, M., Vonsattel, J. P., Wakabayashi, K., & Litvan, I. (2002). Office of Rare Diseases Neuropathologic Criteria for Corticobasal Degeneration. *Journal of Neuropathology and Experimental Neurology*, 61(11), 935–946.  
<https://doi.org/10.1093/jnen/61.11.935>
- Dienel, G. A. (2012). Brain Lactate Metabolism: The Discoveries and the Controversies. *Journal of Cerebral Blood Flow and Metabolism*, 32(7), 1107–1138. <https://doi.org/10.1038/jcbfm.2011.175>
- Dinelle, K., Ngo, H., Blinder, S., Vafai, N., Topping, G., & Sossi, V. (2011). Frame-to-frame image realignment assessment tool for dynamic brain positron emission tomography. *Medical Physics (Lancaster)*, 38(2), 773–781.  
<https://doi.org/10.1118/1.3537289>
- Dubois, B., Feldman, H. H., Jacova, C., Hampel, H., Molinuevo, J. L., Blennow, K., DeKosky, S. T., Gauthier, S., Selkoe, D., Bateman, R., Cappa, S., Crutch, S., Engelborghs, S., Frisoni, G. B., Fox, N. C., Galasko, D., Habert, M.-O., Jicha, G. A., Nordberg, A., ... Cummings, J. L. (2014). Advancing research diagnostic criteria for Alzheimer's disease: the IWG-2 criteria. *Lancet Neurology*, 13(6), 614–629.  
[https://doi.org/10.1016/S1474-4422\(14\)70090-0](https://doi.org/10.1016/S1474-4422(14)70090-0) Eidelberg, D., Moeller, J., R., Kazumata, K., Antonini, A., Sterio, D., Dhawan, V., Spetsieris, P., Alterman, R., Kelly, P. J., Dogali, M., Fazzini, E., & Beric, A. (1997). Metabolic correlates of pallidal neuronal activity in Parkinson's disease. *Brain*, 120(8), 1315–1324.  
<https://doi.org/10.1093/brain/120.8.1315>

- Eidelberg, D., Moeller, J. R., Dhawan, V., Spetsieris, P., Takikawa, S., Ishikawa, T., Chaly, T., Robeson, W., Margouleff, D., Przedborski, S., & Fahn, S. (1994). The Metabolic Topography of Parkinsonism. *Journal of Cerebral Blood Flow and Metabolism*, 14(5), 783–801. <https://doi.org/10.1038/jcbfm.1994.99>
- Fahn, S., Elton, R. L., & UPDRS Program Members. (1987). Unified Parkinson's disease rating scale. In S. Fahn, C. D. Marsden, M. Goldstein, & D. B. Calne (Eds.), *Recent developments in Parkinson's disease* (Vol. 2, pp. 153–163, 293–304). Macmillan Health Care Information.
- Feany, M. B., & Dickson, D. W. (1995). Widespread cytoskeletal pathology characterizes corticobasal degeneration. *The American journal of pathology*, 146(6), 1388.
- Folstein, M. F., Folstein, S. E., & McHugh, P. R. (1975). "Mini-mental state": A practical method for grading the cognitive state of patients for the clinician. *Journal of Psychiatric Research*, 12(3), 189–198. [https://doi.org/10.1016/0022-3956\(75\)90026-6](https://doi.org/10.1016/0022-3956(75)90026-6)
- Friston, K. J., Holmes, A. P., Worsley, K. J., Poline, J.-P., Frith, C. D., & Frackowiak, R. S. J. (1994). Statistical parametric maps in functional imaging: A general linear approach. *Human Brain Mapping*, 2(4), 189–210.  
<https://doi.org/10.1002/hbm.460020402>
- Goldenberg, G. (1999). Matching and imitation of hand and finger postures in patients with damage in the left or right hemispheres. *Neuropsychologia*, 37(5), 559–566.  
[https://doi.org/10.1016/S0028-3932\(98\)00111-0](https://doi.org/10.1016/S0028-3932(98)00111-0)
- Goldenberg, G. (2013). *Apraxia: the cognitive side of motor control* (1st ed.). Oxford University Press. <https://doi.org/10.1093/acprof:oso/9780199591510.001.0001>
- Goldenberg, G. (2016). Apraxia. In M. Husain & J. M. Schott (Eds.), *Oxford textbook of cognitive neurology and dementia* (pp. 141–151). Oxford University Press.
- Gonzalez Rothi, L. J., Ochipa, C., & Heilman, K. M. (1991). A Cognitive Neuropsychological Model of Limb Praxis. *Cognitive Neuropsychology*, 8(6), 443–458. <https://doi.org/10.1080/02643299108253382>

GraphPad Software. (2023). *GraphPad Prism* (Version 9.5.1) [Computer software].

<https://www.graphpad.com>

Greve, D. N., Svarer, C., Fisher, P. M., Feng, L., Hansen, A. E., Baare, W., Rosen, B., Fischl, B., & Knudsen, G. M. (2014). Cortical surface-based analysis reduces bias and variance in kinetic modeling of brain PET data. *NeuroImage (Orlando, Fla.)*, 92, 225–236. <https://doi.org/10.1016/j.neuroimage.2013.12.021>

Hammers, A., Allom, R., Koepp, M. J., Free, S. L., Myers, R., Lemieux, L., Mitchell, T. N., Brooks, D. J., & Duncan, J. S. (2003). Three-dimensional maximum probability atlas of the human brain, with particular reference to the temporal lobe. *Human Brain Mapping*, 19(4), 224–247. <https://doi.org/10.1002/hbm.10123>

Harris, J. J., Jolivet, R., & Attwell, D. (2012). Synaptic Energy Use and Supply. *Neuron (Cambridge, Mass.)*, 75(5), 762–777.

<https://doi.org/10.1016/j.neuron.2012.08.019>

Herholz, K., Herscovitch, P., & Heiss, W. D. (2004). Imaging brain function. In *NeuroPET: positron emission tomography in neuroscience and clinical neurology* (pp. 143–185). Springer. [https://doi.org/10.1007/978-3-642-18766-7\\_3](https://doi.org/10.1007/978-3-642-18766-7_3)

Hinz, R., & Turkheimer, F. E. (2006). Determination of tracer arrival delay with spectral analysis. *IEEE Transactions on Nuclear Science*, 53(1), 212–219.

<https://doi.org/10.1109/TNS.2005.862982>

Huang, S. C., Phelps, M. E., Hoffman, E. J., Sideris, K., Selin, C. J., & Kuhl, D. E. (1980). Noninvasive determination of local cerebral metabolic rate of glucose in man. *American Journal of Physiology: Endocrinology and Metabolism*, 238(1), E69–E82. <https://doi.org/10.1152/ajpendo.1980.238.1.e69>

Huey, E. D., Pardini, M., Cavanagh, A. L., Wassermann, E. M., Kapogiannis, D., & Grafman, J. (2009). Association of ideomotor apraxia with frontal gray matter volume loss in corticobasal syndrome. *Archives of Neurology*, 66(10), 1279–1284. <https://doi.org/10.1001/archneurol.2009.218>

Jansen, W. J., Ossenkoppele, R., Knol, D. L., Tijms, B. M., Scheltens, P., Verhey, F. R. J., Visser, P. J., Aalten, P., Aarsland, D., Alcolea, D., Alexander, M., Almdahl, I. S.,

Arnold, S. E., Baldeiras, I., Barthel, H., van Berckel, B. N. M., Bibeau, K., Blennow, K., Brooks, D. J., ... Zetterberg, H., & the Amyloid Biomarker Study Group. (2015). Prevalence of cerebral amyloid pathology in persons without dementia: A meta-analysis. *JAMA*, 313(19), 1924–1938

Jenkinson, M., & Smith, S. (2001). A global optimisation method for robust affine registration of brain images. *Medical Image Analysis*, 5(2), 143–156.  
[https://doi.org/10.1016/S1361-8415\(01\)00036-6](https://doi.org/10.1016/S1361-8415(01)00036-6)

Jo, S., Oh, J. S., Cheong, E.-N., Kim, H. J., Lee, S., Oh, M., Kim, J. S., Chung, S. J., Lee, C. S., Kwon, M., Kang, D., & Lee, J.-H. (2021). FDG-PET patterns associated with ideomotor apraxia and imitation apraxia in patients with corticobasal syndrome. *Parkinsonism & Related Disorders*, 88, 96–101.  
<https://doi.org/10.1016/j.parkreldis.2021.06.006>

Josephs, K. A., Whitwell, J. L., Boeve, B. F., Knopman, D. S., Petersen, R. C., Hu, W. T., Parisi, J. E., Dickson, D. W., & Jack Jr, C. R. (2010). Anatomical differences between CBS-corticobasal degeneration and CBS-Alzheimer's disease. *Movement Disorders*, 25(9), 1246–1252.  
<https://doi.org/10.1002/mds.23062>

Khalil, M., Teunissen, C. E., Otto, M., Piehl, F., Sormani, M. P., Gattringer, T., Barro, C., Kappos, L., Comabella, M., Fazekas, F., Petzold, A., Blennow, K., Zetterberg, H., & Kuhle, J. (2018). Neurofilaments as biomarkers in neurological disorders. *Nature Reviews. Neurology*, 14(10), 577–589.  
<https://doi.org/10.1038/s41582-018-0058-z>

Luzzi, S., Provinciali, L., Julien, C., Neary, D., & Snowden, J. (2008). Gesture recognition and production in frontotemporal dementia, semantic dementia and corticobasal degeneration. *Dementia and Geriatric Cognitive Disorders*, 26(5), 467–473.

Magistretti, P. J., & Allaman, I. (2015). A Cellular Perspective on Brain Energy Metabolism and Functional Imaging. *Neuron (Cambridge, Mass.)*, 86(4), 883–901.  
<https://doi.org/10.1016/j.neuron.2015.03.035>

Maher, F. (1995). Immunolocalization of GLUT1 and GLUT3 glucose transporters in primary cultured neurons and glia. *Journal of Neuroscience Research*, 42(4), 459–469. <https://doi.org/10.1002/jnr.490420404>

Malarte, M.-L., Gillberg, P.-G., Kumar, A., Bogdanovic, N., Lemoine, L., & Nordberg, A. (2023). Discriminative binding of tau PET tracers PI2620, MK6240 and RO948 in Alzheimer's disease, corticobasal degeneration and progressive supranuclear palsy brains. *Molecular Psychiatry*, 28(3), 1272–1283.

<https://doi.org/10.1038/s41380-022-01875-2>

Meltzer, C. C., Leal, J. P., Mayberg, H. S., Wagner, H. N., & Frost, J. J. (1990). Correction of PET Data for Partial Volume Effects in Human Cerebral Cortex by MR Imaging. *Journal of Computer Assisted Tomography*, 14(4), 561–570.

<https://doi.org/10.1097/00004728-199007000-00011>

Müller-Gärtner, H. W., Links, J. M., Prince, J. L., Bryan, R. N., McVeigh, E., Leal, J. P., Davatzikos, C., & Frost, J. J. (1992). Measurement of Radiotracer Concentration in Brain Gray Matter Using Positron Emission Tomography: MRI-Based Correction for Partial Volume Effects. *Journal of Cerebral Blood Flow and Metabolism*, 12(4), 571–583. <https://doi.org/10.1038/jcbfm.1992.81>

National Institute for Health and Care Excellence. (2018). *Dementia: Assessment, management and support for people living with dementia and their carers* (NICE guideline NG97). <https://www.nice.org.uk/guidance/ng97>

Nichols, T., & Hayasaka, S. (2003). Controlling the familywise error rate in functional neuroimaging: a comparative review. *Statistical Methods in Medical Research*, 12(5), 419–446. <https://doi.org/10.1191/0962280203sm341ra>.

Ossenkoppele, R., Rabinovici, G. D., Smith, R., Schöll, M., Strandberg, O., Palmqvist, S., Mattsson, N., Jögi, J., Ohlsson, T., Jögi, J., Hansson, O., & for the Alzheimer's Disease Neuroimaging Initiative. (2018). Discriminative accuracy of [18F]flortaucipir positron emission tomography for Alzheimer disease vs other neurodegenerative disorders. *JAMA*, 320(11), 1151–1162.

<https://doi.org/10.1001/jama.2018.12917>

- Oxford Centre for Functional MRI of the Brain (FMRIB). (2023). *FSL FLIRT* (Version 6.0.6.4) [Computer software]. <https://fsl.fmrib.ox.ac.uk/fsl/fslwiki/FLIRT>
- Palop, J. J., Chin, J., & Mucke, L. (2006). A network dysfunction perspective on neurodegenerative diseases. *Nature*, 443(7113), 768–773.  
<https://doi.org/10.1038/nature05289>
- Pardini, M., Huey, E. D., Spina, S., Kreisl, W. C., Morbelli, S., Wassermann, E. M., Nobili, F., Ghetti, B., & Grafman, J. (2019). FDG-PET patterns associated with underlying pathology in corticobasal syndrome. *Neurology*, 92(10), e1121–e1135.  
<https://doi.org/10.1212/WNL.0000000000007038>
- Pauwels, E. K. (2001). 18F-labeled fluorodeoxyglucose for PET imaging: The working mechanism and its clinical implication. *Drugs Future*, 26(7), 659-668.  
<https://doi.org/10.1358/dof.2001.026.07.858710>
- Peigneux, P., Salmon, E., Garraux, G., Laureys, S., Willemans, S., Dujardin, K., Degueldre, C., Lemaire, C., Luxen, A., Moonen, G., Franck, G., Destee, A., & Van der Linden, M. (2001). Neural and cognitive bases of upper limb apraxia in corticobasal degeneration. *Neurology*, 57(7), 1259–1268.  
<https://doi.org/10.1212/WNL.57.7.1259>
- Pellerin, L., & Magistretti, P. J. (1994). Glutamate Uptake into Astrocytes Stimulates Aerobic Glycolysis: A Mechanism Coupling Neuronal Activity to Glucose Utilization. *Proceedings of the National Academy of Sciences - PNAS*, 91(22), 10625–10629. <https://doi.org/10.1073/pnas.91.22.10625>
- Robb, R. A., & Hanson, D. P. (1991). A software system for interactive and quantitative visualization of multidimensional biomedical images. *Australasian Physical & Engineering Sciences in Medicine*, 14(1), 9–30.  
<https://europemc.org/article/med/2029243>
- Rousset, O. G., Ma, Y., & Evans, A. C. (1998). Correction for Partial Volume Effects in PET: Principle and Validation. *The Journal of Nuclear Medicine* (1978), 39(5), 904–911.

Roy, E. A., & Square, P. A. (1985). Common considerations in the study of limb, verbal and oral apraxia. In *Advances in psychology* (Vol. 23, pp. 111-161). North-Holland.

Royall, D. R., Lauterbach, E. C., Cummings, J. L., Reeve, A., Rummans, T. A., Kaufer, D. I., LaFrance, W. C., Jr., & Coffey, C. E. (2002). Executive control function: A review of its promise and challenges for clinical research. A report from the Committee on Research of the American Neuropsychiatric Association. *Journal of Neuropsychiatry and Clinical Neurosciences*, 14(4), 377–405. <https://doi.org/doi:10.1176/appi.neuropsych.14.4.377>

Sakurada, O., & Shinohara, M. (1977). The [14C]deoxyglucose method for the measurement of local cerebral glucose utilization: theory, procedure, and normal values in the conscious and anesthetized albino rat. *Journal of Neurochemistry*, 28(5), 897. <https://doi.org/10.1111/j.1471-4159.1977.tb10649.x>

Schmidt, K., Lucignani, G., Moresco, R. M., Rizzo, G., Gilardi, M. C., Messa, C., Colombo, F., Fazio, F., & Sokoloff, L. (1992). Errors Introduced by Tissue Heterogeneity in Estimation of Local Cerebral Glucose Utilization with Current Kinetic Models of the [18F]Fluorodeoxyglucose Method. *Journal of Cerebral Blood Flow and Metabolism*, 12(5), 823–834.

<https://doi.org/10.1038/jcbfm.1992.114>

Schmidt, K., Mies, G., & Sokoloff, L. (1991). Model of Kinetic Behavior of Deoxyglucose in Heterogeneous Tissues in Brain: A Reinterpretation of the Significance of Parameters Fitted to Homogeneous Tissue Models. *Journal of Cerebral Blood Flow and Metabolism*, 11(1), 10–24. <https://doi.org/10.1038/jcbfm.1991.2>

Senjem, M. L., Gunter, J. L., Shiung, M. M., Petersen, R. C., & Jack, C. R. (2005). Comparison of different methodological implementations of voxel-based morphometry in neurodegenerative disease. *NeuroImage*, 26(2), 600–608. <https://doi.org/10.1016/j.neuroimage.2005.02.005>

Shidahara, M., Thomas, B. A., Okamura, N., Ibaraki, M., Matsubara, K., Oyama, S., Ishikawa, Y., Watanuki, S., Iwata, R., Furumoto, S., Tashiro, M., Yanai, K., Gonda,

K., & Watabe, H. (2017). A comparison of five partial volume correction methods for Tau and Amyloid PET imaging with [18F]THK5351 and [11C]PIB. *Annals of Nuclear Medicine*, 31(7), 563–569. <https://doi.org/10.1007/s12149-017-1185-0>

Shir, D., Thu Pham, N. T., Botha, H., Koga, S., Kouri, N., Ali, F., Knopman, D. S., Petersen, R. C., Boeve, B. F., Kremers, W. K., Nguyen, A. T., Murray, M. E., Reichard, R. R., Dickson, D. W., Graff-Radford, N., Josephs, K. A., Whitwell, J., & Graff-Radford, J. (2023). Clinicoradiologic and Neuropathologic Evaluation of Corticobasal Syndrome. *Neurology*, 101(3), e289–e299. <https://doi.org/10.1212/WNL.0000000000207397>

Sokoloff, L. (1977). Relation Between Physiological Function And Energy Metabolism In The Central Nervous System. *Journal of Neurochemistry*, 29(1), 13–26. <https://doi.org/10.1111/j.1471-4159.1977.tb03919.x>

Soret, M., Bacharach, S. L., & Buvat, I. (2007). Partial-Volume Effect in PET Tumor Imaging. *The Journal of Nuclear Medicine* (1978), 48(6), 932–945. <https://doi.org/10.2967/jnmed.106.035774>

Tapiola, T., Alafuzoff, I., Herukka, S. K., Parkkinen, L., Hartikainen, P., Soininen, H., & Pirtilä, T. (2009). Cerebrospinal fluid β-amyloid 42 and tau proteins as biomarkers of Alzheimer-type pathologic changes in the brain. *Archives of neurology*, 66(3), 382-389

The MathWorks, Inc. (2024). MATLAB (Version R2024a) [Computer software]. <https://www.mathworks.com/>

Thomas, B. A., Erlandsson, K., Modat, M., Thurfjell, L., Vandenberghe, R., Ourselin, S., & Hutton, B. F. (2011). The importance of appropriate partial volume correction for PET quantification in Alzheimer's disease. *European Journal of Nuclear Medicine and Molecular Imaging*, 38(6), 1104–1119. <https://doi.org/10.1007/s00259-011-1745-9>

Valk, P. E., Bailey, D. L., Townsend, D. W., & Maisey, M. N. (2003). Positron emission tomography. *Springer-Verlag London*, 1, 5.

Walker, M. D., Asselin, M.-C., Julyan, P. J., Feldmann, M., Talbot, P. S., Jones, T., & Matthews, J. C. (2011). Bias in iterative reconstruction of low-statistics PET data: benefits of a resolution model. *Physics in Medicine & Biology*, 56(4), 931–949.  
<https://doi.org/10.1088/0031-9155/56/4/004>

Wellcome Trust Centre for Neuroimaging. (2014). SPM12 [Computer software].  
<https://www.fil.ion.ucl.ac.uk/spm/>

Whitwell, J. L., Jack, C. R., Boeve, B. F., Parisi, J. E., Ahlskog, J. E., Drubach, D. A., Senjem, M. L., Knopman, D. S., Petersen, R. C., Dickson, D. W., & Josephs, K. A. (2010). Imaging correlates of pathology in corticobasal syndrome. *Neurology*, 75(21), 1879–1887.  
<https://doi.org/10.1212/WNL.0b013e3181feb2e8>

Wilburn, M. W., & Kesner, R. P. (1974). Effects of caudate nucleus stimulation upon initiation and performance of a complex motor task. *Experimental Neurology*, 45(1), 61–71. [https://doi.org/10.1016/0014-4886\(74\)90100-9](https://doi.org/10.1016/0014-4886(74)90100-9)

Zimmer, E. R., Parent, M. J., Souza, D. G., Leuzy, A., Lecrux, C., Kim, H.-I., Gauthier, S., Pellerin, L., Hamel, E., & Rosa-Neto, P. (2017). [18F]FDG PET signal is driven by astroglial glutamate transport. *Nature Neuroscience*, 20(3), 393–395.  
<https://doi.org/10.1038/nn.4492>